이학박사 학위논문

Hetero-interfacial control of electronic structures in perovskite ultrathin ruthenates

페로브스카이트 초박막 루테늄에서의 전자 구조에 대한 계면 제어

2022 년 8 월

서울대학교 대학원

물리천문학부

고 은 교

Hetero-interfacial control of electronic structures in perovskite ultrathin ruthenates

Eun Kyo Ko

Supervised by

Professor Tae Won Noh

A Dissertation Submitted to the Faculty of Seoul National University in Partial Fulfillment of the Requirements for the Degree of Doctor of Philosophy

August 2022

Department of Physics and Astronomy

Graduate School

Seoul National University

Hetero-interfacial control of electronic structures in perovskite ultrathin ruthenates

페로브스카이트 초박막 루테늄에서의 전자 구조에 대한 계면 제어

지도교수 노 태 원

이 논문을 이학박사학위논문으로 제출함
2022 년 6 월

서울대학교 대학원
물리·천문학부
고 은 교

고은교의 박사학위논문을 인준함
2022 년 6 월

위 원 장 **최 석 봉** (인)
부 위 원 장 **노 태 원** (인)
위 원 **장 준 호** (인)
위 원 **이 승 섭** (인)
위 원 **장 서 형** (인)

Contents

List of Figures iv

Abstract xiii

Chapter 1. Introduction 1

1.1 Transition metal oxides

1.2 Hetero-interfacial engineering

1.3 Perovskite 4*d* ruthenates

1.4 Outline of Thesis

Chapter 2. Experimental Methods 16

2.1 Pulsed laser deposition

2.2 Transport measurements

2.3 Magnetization measurements

2.4 Angle-resolved photoemission spectroscopy

2.5 Spectroscopic ellipsometry

Chapter 3. Orbital-selective phase transition in a two-dimensional correlated system 29

3.1 Introduction

3.1.1 Hund's rule coupling in perovskites

3.1.2 Symmetry-preserving strain engineering of $SrRuO_3$ monolayer

3.2 Structural characterization

3.3 Control of the electronic structure of the $SrRuO_3$ monolayer

3.4 Interatomic optical transitions and filling control

3.5 Conclusion

Chapter 4. Hetero-interfacial control for oxygen vacancy migration 47

4.1 Introduction

4.1.1 Oxygen vacancies in transition metal oxides

4.1.2 Oxygen vacancy migration to $SrRuO_3$ ultrathin films

4.1.3 Control of kinetic energy of ions during pulsed laser deposition

4.2 Oxygen vacancy in $SrRuO_3$

4.3 Control of ferromagnetic coercive field

4.4 Conclusion

Chapter 5. Hetero-interfacial control for two-channel anomalous Hall effect.....70

5.1 Introduction

5.1.1 Berry curvatures and anomalous Hall effect in $SrRuO_3$

5.2 Two different magnetic phases and two-channel anomalous Hall

effect
5.3 Magnetic inhomogeneity induced during heterostructure engineering
5.4 Conclusion

Chapter 6. Summary and Outlook.....88

List of Publication 92

국문 초록 (Korean Abstract) 97

List of Figures

Fig. 1-1 Radial distribution functions depending on distance (r) and effectively nuclear charge (Z). According to the atomic row of the *d*-block, the distribution function varies. From 3*d* to 5*d*, the *d*-orbital becomes more extended. Adapted from [1].

.

Fig. 1-2 Spectral density for several value of *U/W* obtained from calculation. The first four states are correlated metals, and then there is a Mott transition. Adapted from [2].

Fig. 1-3 Degree of correlations (quasiparticle weight) for three-orbital model to describe TMOs. Black bars indicate Mott states, while white arrows indicate the direction where *J* increases. X marks are the states where $J = 0$. For half-filled system, large *J* value helps to stabilize Mott phase. On the other hand, for non-half-filled system, large *J* value hampers to form Mott phase while decreasing quasiparticle weight. Adapted from [3].

Fig. 1-4 Symmetries and degrees of freedom of correlated electrons. Emergent phenomena can be induced from interplay between them in TMOs. Adapted from [4].

Fig. 2-1 **a** The intensity of reflection high energy electron diffraction (RHEED) during $SrRuO_3$ (SRO) growth. During the first- and second-layer, it shows layer-by-layer growth. After that, it shows step flow growth. For precise

thickness control, the total pulse number is calculated based on the first and second oscillation. **b** Intensity of RHEED during $LaAlO_3$ (LAO) growth, showing layer-by-layer growth mode. **c-e** RHEED patterns after growth of SRO (**c**), LAO (5 mTorr)/SRO (**d**), and LAO (0.5 mTorr)/SRO (**e**) on $SrTiO_3$(001; STO) substrate. Adapted from E. K. Ko *et al* (2022).

Fig. 2-2 Optical microscopic image of 50×50 μm^2 Hall bar. The scale bar indicates 50 μm. Adapted from [5].

Fig. 2-3 We extracted the OHE part by linear fitting. Adapted from [6].

Fig. 2-4 ARPES technique. When electron absorb photon, it is emitted into vacuum. By analyzing the emitted angles, angle-resolved momentum in the x and y directions can be collected. Adopted from [7].

Fig. 3-1 Crystal field splitting of d-orbitals due to oxygen octahedron in perovskites.

Fig. 3-2 Map for degree of correlations for partially occupied three t_{2g} orbitals. The white arrow indicates direction of increasing J. The black bar indicates Mott state. For 3-orbital/3-electron system (half-filled), J helps to open the Mott gap. Adapted from [3].

Fig. 3-3 Symmetry-preserving strain engineering on SRO monolayer.

Fig. 3-4 Structural characterization for SRO heterostructures. Low-energy electron diffraction patterns for SRO monolayers shows symmetry-preserving strain engineering were successful. STEM images indicate high-quality of SRO single layer. Occasionally, we observed small regions with thickness

inhomogeneity.

Fig. 3-5 Metal-to-insulator transition induced by epitaxial strain in SRO monolayers.

Fig. 3-6 Interatomic optical transitions in SRO and optical spectra obtained by spectroscopic ellipsometry.

Fig. 4-1 Schematics of oxygen vacancy (V_O) configuration in $SrTiO_3/SrRuO_3/SrTiO_3$(001) [STO/SRO/STO(001)] heterostructures during pulsed laser deposition (PLD). The red dots in $SrTiO_{3-\delta}$ and $SrRuO_{3-\delta}$ indicate V_O. a Oxygen deficient $SrTiO_{3-\delta}$ film was deposited on an SRO film. V_O in the STO capping layer migrates into the SRO layer underneath during deposition, resulting in oxygen deficient $SrRuO_{3-\delta}$. b The formation energy of V_O is plotted according to the position of V_O in the STO/SRO heterostructure. The black arrows indicate V_O migration from the capping STO into the underlying SRO. Adapted from [6].

Fig. 4-2 Investigation of V_O in SRO by scanning transmission electron microscopy (STEM). **a, b** Atomically resolved annular bright-field (ABF) images of (**a**) STO/SRO thin films where the oxygen partial pressure during the STO capping layer deposition [$P(O_2)_{STO}$] is 100 mTorr [STO(100 mTorr)/SRO] and (**b**) 5 mTorr [STO(5 mTorr)/SRO]. The SRO layer in (**a**) has uniform intensity contrast whereas (**b**) shows obvious contrast variations, suggesting the existence of defects in STO(5 mTorr)/SRO **c**, **d**) Magnified images of preselected regions in (**a**) and (**b**) (dashed boxes). **e-h**) Inverted intensity line profiles extracted from vertical and horizontal BO_2 (TiO_2 or RuO_2) atomic planes. The high intensity peaks indicate heavy cations such as Ru

(solid brown circles) and Ti (solid green circles). The peaks of much lower intensity indicate oxygen sites (solid red circles). For both samples, the clear peaks of all of the cation and oxygen in STO(001) and STO suggest few cation vacancies and V_O in the substrate and STO layer. In contrast, the intensity of oxygen peaks of SRO fluctuates in STO(5 mTorr)/SRO as shown in (**g**), and (**h**), whereas the oxygen peaks of SRO in STO(100 mTorr)/SRO are still uniform, as indicated in (**e**), and (**f**). The non-uniform and weak intensity of oxygen sites in STO(5 mTorr)/SRO suggest a high-density of V_O (open black circles). Adapted from [6].

Fig. 4-3 Investigation of structural distortion in SRO by STEM. **a, b** High angle annular dark-field (HAADF) images of (**a**) STO(100 mTorr)/SRO and (**b**) STO(5 mTorr)/SRO. **c, d** Integrated ratio of the *c*-lattice of the bilayers to the in-plane lattice constant of the substrate (c/a_{subs}). Note that the maximum of c/a_{subs} in SRO is 102 % in STO(100 mTorr)/SRO, and 105 % in STO(5 mTorr)/SRO. The predicted c/a_{subs} of compressively-strained SRO thin film on STO(001), according to the Poisson ratio, is denoted by the dashed line in (**c**), (**d**). The significant increase of c/a_{sub} in STO(5 mTorr)/SRO compared to STO(100 mTorr)/SRO suggests that high V_o concentration expends the unit-cell volume. Adapted from [6].

Fig. 4-4 Transport and magnetization measurement of STO/SRO thin films. **a** Temperature-dependent longitudinal transport (ρ_{xx}-T) measurement of STO(100 mTorr)/SRO and STO(5 mTorr)/SRO. **b** Temperature-dependent magnetization (M-T) measurement of STO(100 mTorr)/SRO and STO(5 mTorr)/SRO. The Curie temperature (T_C) of the ferromagnetic transition is indicated by the kinks in ρ_{xx}-T and M-T. T_C of both films is about 150 K.

Adapted from [6].

Fig. 4-5 The variation of the coercive field (H_C) with thickness of capping STO (t_{STO}) and $P(O_2)_{STO}$. **a** Normalized H-dependent anomalous Hall resistivity (ρ_{AHE}-H) measured at 5 K in STO(100 mTorr)/SRO for different t_{STO}. There is little change of H_C with t_{STO}. **b** Normalized ρ_{AHE}-H measured at 5 K in STO(5 mTorr)/SRO for different t_{STO}. Contrary to (**a**), there is a large increase of H_C as t_{STO} increases. c) t_{STO} dependent H_C of STO/SRO with $P(O_2)_{STO}$ = 100 mTorr (solid blue circles) and $P(O_2)_{STO}$ = 5 mTorr (solid red circles). H_C decreases slightly as t_{STO} increases for $P(O_2)_{STO}$ = 100 mTorr, whereas H_C gradually increases from 1.6 to 4.8 T and then saturates for $P(O_2)_{STO}$ = 5 mTorr. **d** Normalized ρ_{AHE}-H measured at 5 K in STO (t_{STO}=3 u.c.)/SRO with different $P(O_2)_{STO}$. H_C greatly increases for decreasing $P(O_2)_{STO}$. **e** $P(O_2)_{STO}$ dependent H_C of SRO. H_C varies significantly by changing $P(O_2)_{STO}$. Adapted from [6].

Fig. 4-6 Measurement of magnetic anisotropy by field-angle dependent Hall effect. **a** Experimental geometry of field-angle dependent Hall resistivity (ρ_{xy}). The angle between the external field (H) and [001] axis is denoted as θ. **b, c** The field angle dependent Hall resistivity (θ-ρ_{xy}) of (**b**) STO(100 mTorr)/SRO and (**c**) STO(5 mTorr)/SRO(5 u.c.) at 5 K. A constant H rotates both clockwise and anticlockwise. **d, e** Schematic magnetization configurations of SRO when (**d**) H is much smaller than the anisotropy field (H_A) and (**e**) H is comparable to H_A. When $H<<H_A$, the magnetization aligns with the film normal, showing a large hysteresis area with sharp magnetic switching. By contrast, when H is comparable to H_A, the spin will continuously reorient along the H direction, showing a smaller hysteresis area and smooth magnetic switching. **f, g** $d\rho_{xy}/d\theta$ - θ curves when (**f**) $H<<H_A$ [H = 3T

for STO(100 mTorr)/SRO] and (**g**) $H \sim H_A$ [H =14T for STO(100 mTorr)/SRO]. $\Delta\theta_{flipping}$ is the difference in θ where magnetic switching occurs. ρ_{slope} is the peak value of $d\rho_{xy}/d\theta$. **h** H dependent $\Delta\theta_{flipping}$ of both samples. **i** Normalized H dependent ρ_{slope} for both films. The larger values of both $\Delta\theta_{flipping}$ and ρ_{slope} for STO(5 mTorr)/SRO at high H indicate that H_A of STO(5 mTorr)/SRO is larger than that of STO(100 mTorr)/SRO. Adapted from [6].

Fig. 5-1 Field-dependent anomalous Hall resistivity (ρ_{AHE}-H) curves and temperature-dependent magnetization (M-T) curves of $SrRuO_3$ (SRO) and $LaAlO_3$ (LAO)-capped SRO films. **a** 5 u.c.-SRO films and with and without the capping layers. **b** Optical microscopic image of 50×50 ic^2 Hall bar. The scale bar indicates 50 μm. **c** ρ_{AHE}-H curves of 5 u.c.-SRO films without capping layers measured at 10 K. All linear terms from the ordinary Hall effect have been subtracted. **d** M-T curves of 5 u.c.-SRO films without capping layers. The black solid lines are the experimental data and the grey solid lines are the first derivative curves. **e-g** ρ_{AHE}-H curves of LAO-capped SRO films. The growth conditions and thicknesses of the SRO layers were fixed while the oxygen pressure during LAO layer growth [$P(O_2)_{LAO}$] was varied from 5 to 0.5 mTorr. **h-j** M-T curves of LAO-capped SRO films. The blue (red) dotted lines were derived at Curie temperatures (T_C) of ~120 K (~90 K). Adapted from [5].

Fig. 5-2 Scanning transmission electron microscopy (STEM) images, obtained in annular bright-field (ABF) mode, of LAO-capped SRO films, and their time-of-flight secondary ion mass spectra (TOF-SIMS). **a, b** STEM images of LAO-capped SRO when $P(O_2)_{LAO}$ = 5 mTorr (**a**) and 0.5 mTorr (**b**). **c** Enlarged image of the blue dashed square in (**a**). **d** Enlarged images of the red dashed square in (**b**). The atomic positions of cations and oxygens are

well-defined in the $P(O_2)_{LAO}$ = 5 mTorr sample, but not in the $P(O_2)_{LAO}$ = 0.5 mTorr sample. The elongation and uncertainty of positioning is highlighted in red dashes. **e** Depth profile of the TOF-SIMS. The blue solid line is that from the $P(O_2)_{LAO}$ = 5 mTorr sample and the red solid line indicates the $P(O_2)_{LAO}$ = 0.5 mTorr sample. The grey areas indicate differences between the samples. The grey digits indicate the proportions of grey areas, as revealed by the integrated TOF spectra from the 5-mTorr sample. Ru deficiency is mainly observed in the SRO layer. Adapted from [5].

Fig. 5-3 Fitted *M-T* curves and ρ_{AHE}-*H* values of LAO-capped SRO samples, and the ratios of the 90 K phase. **a–e** Fitted *M-T* curves of LAO-capped SRO samples with $P(O_2)_{LAO}$ values of 50 (**a**), 7 (**b**), 5 (**c**), 1 (**d**), and 0.5 mTorr (**e**). The red and blue curves are fitting curves at T_C values of 90 and 120 K, respectively. Black open circles are experimental results and the green lines are the summations of the fitting curves. **f–j** The fitted ρ_{AHE}-*H* curves of LAO-capped SRO samples when the LAO layer growth pressures were 50 (**f**), 7 (**g**), 5 (**h**), 1 (**i**), and 0.5 mTorr (**j**). The red and blue curves are negative ($\rho_{(-)}$) and positive ($\rho_{(+)}$) fitting curves. **k** The total pressure during capping layer growth (P_{total}) affects the 90 K phase ratios extracted from the fittings. The black circles are the ratios extracted from ρ_{AHE}-*H* curves and the orange circles are the ratios extracted from *M-T* curves. The solid lines are the results obtained when the LAO capping layers were grown under only oxygen pressure. The dashed line indicates the ratios of samples for which the LAO capping layers were grown in a mixture of argon and oxygen. As the $P(O_2)_{LAO}$ decreases, the 90 K phase ratio increases. Adapted from [5].

Fig. 5-4 Schematics of PLD kinetics according to the background pressure, and a control experiment with total pressure variation during growth of the LAO

capping layer. **a** At high pressure, the kinetic energy of the evaporated plume is suppressed. **b** At low pressure, the high kinetic energy of the evaporated plume induces SRO film inhomogeneities. The red regions in the SRO layer re inhomogeneous phases caused by the high kinetic energy of the adatoms. **c** The red regions in the SRO film exhibit positive AHEs, as shown by the hump signals in the ρ_{AHE}-H curve. **d–g** ρ_{AHE}-H curves derived by varying P_{Total} from 15 to 0.5 mTorr. The O_2 partial pressure is fixed at 0.5 mTorr; only the Ar partial pressure is varied. The black open circles are the experimental curves and the red and blue curves the $\rho_{(-)}$- and $\rho_{(+)}$-fitting curves. The gray lines are the summations of the fitting curves. As P_{Total} decreases, $\rho_{(+)}$ increases. Adapted from [5].

Fig. 5-5 Temperature dependence of magnetization (M-T) of a control experiment with total pressure (P_{total}) variation during the growth of the LAO capping layer. P_{Total} is varied from 15 mTorr to 0.5 mTorr. The O_2 partial pressure is fixed as 0.5mTorr, while Ar partial pressure is only varied. Adapted from [5].

References

1. Martins, C., Aichhorn, M. & Biermann, S. Coulomb correlations in 4d and 5d oxides from first principles - Or how spin-orbit materials choose their effective orbital degeneracies. *J. Phys. Condens. Matter* **29**, (2017).
2. George, A., Kotliar, G., Krauth, W. & Rozenberg, M. J. Dynamical mean-field theory of strongly correlated fermion systems and the limit of infinite dimensions. *J. Mol. Neurosci.* **35**, 91–100 (2008).
3. Georges, A., De Medici, L. & Mravlje, J. Strong correlations from hund's coupling. *Annu. Rev. Condens. Matter Phys.* **4**, 137–178 (2013).
4. Hwang, H. Y. *et al.* Emergent phenomena at oxide interfaces. *Nat. Mater.* **11**, 103–113 (2012).
5. Ko, E. K. *et al.* Tunable Two-Channel Magnetotransport in SrRuO3 Ultrathin Films Achieved by Controlling the Kinetics of Heterostructure Deposition. *Adv. Electron. Mater.* **8**, 1–8 (2022).
6. Ko, E. K. *et al.* Oxygen Vacancy Engineering for Highly Tunable Ferromagnetic Properties: A Case of SrRuO3 Ultrathin Film with a SrTiO3 Capping Layer. *Adv. Funct. Mater.* **30**, 2001486 (2020).
7. Yang, H. *et al.* Visualizing electronic structures of quantum materials by angle-resolved photoemission spectroscopy. *Nat. Rev. Mater.* **3**, 341–353 (2018).

Abstract

Hetero-interfacial control of electronic structures in perovskite ultrathin ruthenates

Eun Kyo Ko
Department of Physics and Astronomy
Graduate School, Seoul National University, Seoul, Korea

Quantum materials host a variety of phenomena beyond the single-electron band theory. As strongly correlated systems, transition metal oxides (TMOs) exhibit exotic features including ferromagnetism, and unconventional superconductivity. Among TMOs, 4*d* ruthenates have been extensively studies due to their fine balance between electronic correlations. In such systems, the energy scales of on-site Coulomb interaction (*U*), Hund's rule coupling (*J*), and spin-orbital coupling are comparable, giving rise to a variety of functionalities. In this dissertation, we control the electronic structures of perovskite ruthentates ultrathin films by interfacial engineering.

First, we investigate the orbital-selective phases in $SrRuO_3$ (SRO) monolayers via epitaxial strain engineering. Despite vast previous theoretical studies on Hund-driven

physics, experimental confirmation has been rare due to experimental difficulties. Here, we demonstrate an experimental method to systematically investigate physics in Hund's systems. The epitaxial strains modulate tetragonal crystal field, which effectively vary the orbital occupancies. Following the ambient nature of *J*, we observe a drastic change in electronic sturctures; a metal-insulator transition with an orbital differentiation confirmed by *in-situ* angle-resolved photoemission spectroscopy. We provide a practical direction for exploring multi-orbital physics as well as device applications in Hund's systems.

Second, we discuss the ferromagnetic properties of ultrathin SRO with oxygen vacancy (V_O). In TMOs, control of V_O can give rise to many intriguing physical properties. However, inducing V_O in SRO has been challenging due to volatility of Ru. Here, we utilize interfacial engineering for V_O migration. By changing the growth pressure during the $SrTiO_3$ (STO) capping layer deposition, the kinetic energy of ions arriving to the bottom SRO layer can be controlled. The high kinetic process of pulsed laser deposition (PLD) can overcome the migration energy barrier at STO/SRO and V_O can be migrated into SRO. We observe V_O in SRO and structural modification in SRO such as *c*-lattice expansion near the interface. Following, a continuous control of ferromagnetic coercive field of ultrathin SRO is achieved by controlling the amount of V_O migration. We conclude that the large amount of V_O induces enhancement of perpendicular magnetic anisotropy, resulting in increasing coercive field.

Lastly, we investigate multiple anomalous Hall effect (AHE) interpretation in ultrathin SRO films by inducing different magnetic phases. We control the growth

pressure during the $LaAlO_3$ capping layer growth for control of the kinetic process during PLD. According to the growth pressure, two different magnetic phases in ultrathin SRO films are induced, and the composition between them can be systematically controlled. We find that the amplitude and sign of AHE change according to the composition of the magnetic phases. Our results indicate that the Berry curvature-driven AHE in ultrathin SRO films is strongly related to its magnetic properties.

Keywords: transition metal oxides, epitaxial strain engineering, interfacial engineering, electronic structure, Hund's rule coupling, Mott transition, metal-insulator transition, oxygen vacancy, ferromagnetism, anomalous Hall effect.

Student number: 2017-2668

Chapter 1
Introduction

In this chapter, we discuss motivation for studying physical properties of transition metal oxides. We introduce the background information for electronic correlations and functional properties in transition metal oxides, and hetero-interfacial engineering method for exploring physical properties, particularly on perovskite 4*d* ruthenates. In the end of the chapter, we summarize the outline of the thesis.

1.1 Transition metal oxides

Transition metal oxides (TMOs) are quantum materials which have partially-filled *d* orbitals. They host rich phases and functional properties including unconventional superconductivity, ferroelectricity, and ferromagnetism. Mainly due to the orbital size, the energy scales of electronic correlations, such as on-site Coulomb interaction (*U*), Hund's rule coupling (*J*), and spin-orbit coupling (SOC), are determined. The radial distribution as distance from the nucleus varies depending on the atomic row and nuclear charge (Z) (**Fig. 1-1**). For example, due to smaller size of *d* orbitals in 3*d* TMOs, they have larger *U* value compared to those of 4*d* and 5*d* TMOs.

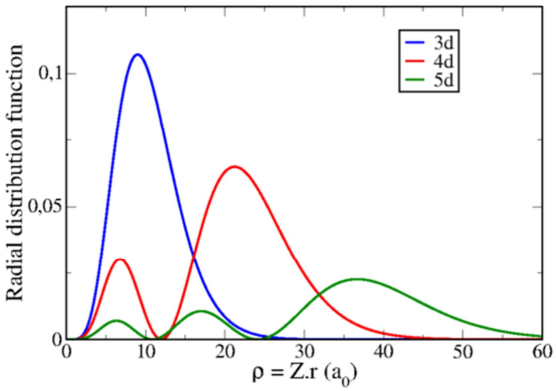

Fig. 1-1. Radial distribution functions depending on distance (r) and effectively nuclear charge (Z). According to the atomic row of the *d*-block, the distribution function varies. From 3*d* to 5*d*, the *d*-orbital becomes more extended. Adapted from [1].

In correlated physics, U has been central paradigm since the discovery of Mott transition. The insulating states in 3d TMOs, which cannot be described by single-band theory, have been understood by Hubbard model. The charge transfer can be modulated determining the charge-localized phases in the odd number of electrons per unit cell, considering the electronic correlation, U. Interestingly, the electron hopping term can be modulated in TMOs by changing lattice, which tunes the bandwidth (W). On this basis, tremendous researches on metal-insulator transition (MIT) with "U vs. W" have been studied in TMOs (**Fig. 1-2**).

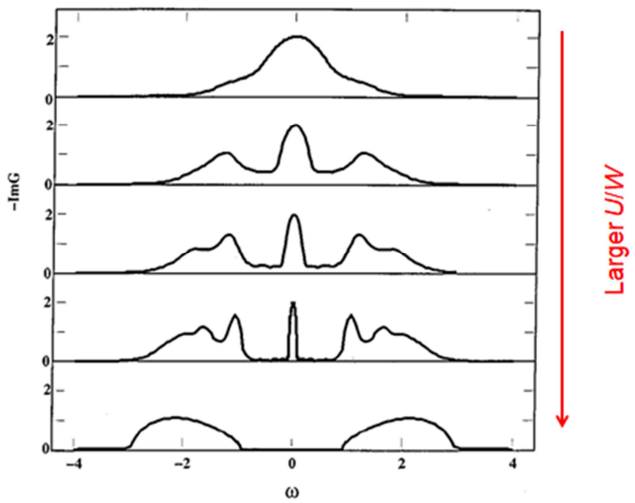

Fig. 1-2. Spectral density for several value of *U/W* obtained from calculation. The first four states are correlated metals, and then there is a Mott transition. Adapted from [2].

J, another electron correlation, plays important role especially for determining phases in multi-orbital systems. In multi-orbital systems, electron distribution follows the Hund's rules: 1. maximize total spin, 2. maximize total angular momentum. Therefore, *J* regulates spin directions as well as charge transfer. With development numerical methods of dynamical mean field theory, the *J*-driven correlated phases have been investigated (**Fig. 1-3**). Interestingly, phase transitions can be induced with small controls in Hund's system due to the ambivalent nature of *J*.

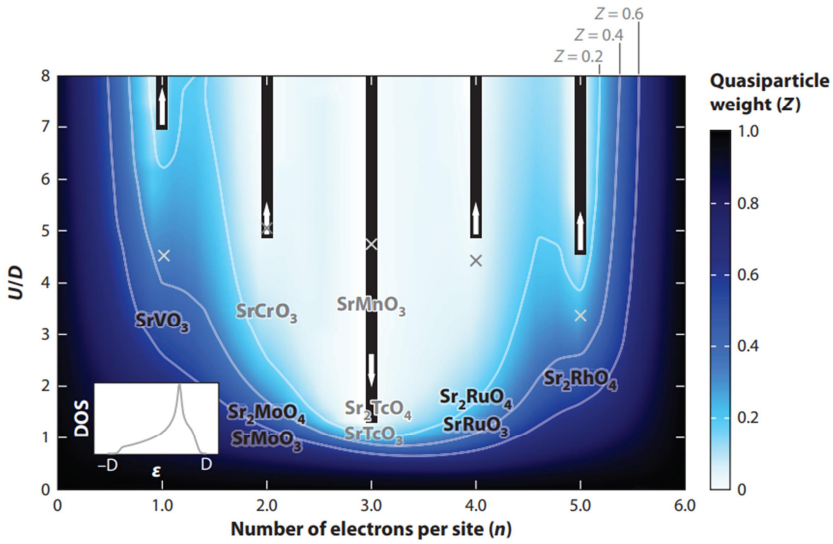

Fig. 1-3. Degree of correlations (quasiparticle weight) for three-orbital model to describe TMOs. Black bars indicate Mott states, while white arrows indicate the direction where *J* increases. X marks are the states where $J = 0$. For half-filled system, large *J* value helps to stabilize Mott phase. On the other hand, for non-half-filled system, large *J* value hampers to form Mott phase while decreasing quasiparticle weight. Adapted from [3].

On top of the electronic correlations, the symmetry of the order parameter such as spatial-inversion or time-reversal symmetry should be considered in TMOs. For example, the breaking of spatial-inversion symmetry is requirement for ferroelectricity. The breaking of time-reversal symmetry in ferromagnetic ordering systems has non-trivial Berry curvatures. Therefore, understanding the interplay between the symmetry and electronic correlations is a key for a comprehensive understanding of intriguing phenomena in TMOs (**Fig. 1-4**).

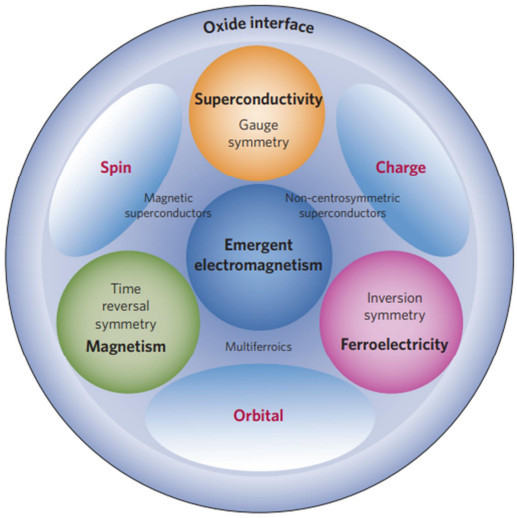

Fig. 1-4. Symmetries and degrees of freedom of correlated electrons. Emergent phenomena can be induced from interplay between them in TMOs. Adapted from [4].

1.2 Hetero-interfacial engineering

The oxide heterostructure, where two different oxides are adjacent, novel electronic states can be emerged. By utilizing interactions between lattice, charge, orbital, and spin degrees of freedom, new electronic states can be stabilized at the heterointerfaces (**Fig. 1-5**)[5]. First, due to the structural proximity effect, the lattice can be modulated compared to the bulk system. Therefore, it can stabilize metastable phases [6,7]. Second, two-dimensional electronic states can be forms at the heterointerfaces. Metallic or superconducting states can emerge between two insulating phases[4,8]. Third, the strain can squeeze or elongate oxygen environments in TMOs, breaking orbital degeneracy. The orbital degeneracy lifting can redistribute electrons, giving different phases. Lastly, there can be exchange bias between ferromagnetic and antiferromagnetic interfaces[9].

It is worthy to note that the hetero-interfacial engineering has less disorder problem compared to doping experiments[5]. The chemical doping always has disorder problem such as cation mixing. Therefore, the hetero-interfacial engineering has great opportunities for studying relationship between electronic correlations and physical properties.

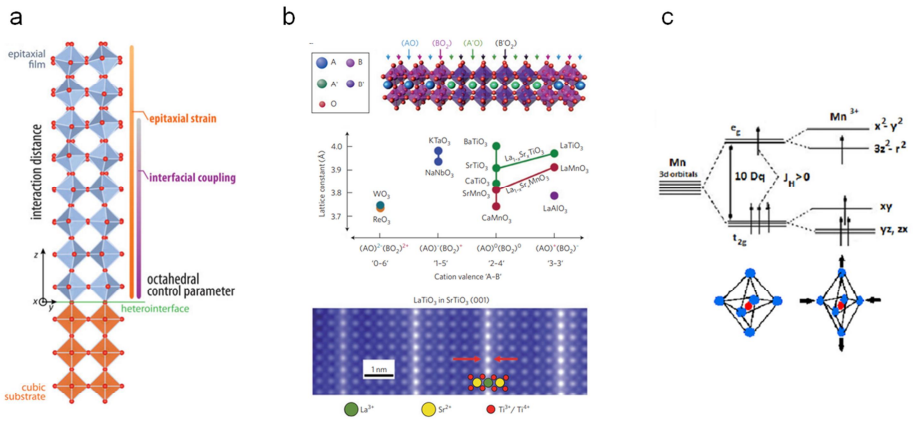

Fig. 1-5. New electronic states stabilized at the heterointerfaces. **a.** lattice modulation at the heterointerfaces, including epitaxial strains and oxygen octahedral connectivity controls. Adapted from [10]. **b.** charge modulation at the heterointerfaces. Adapted from [4]. **c.** orbital degeneracy lifting due to epitaxial strains. Adapted from [11].

1.3 Perovskite 4*d* ruthenates

The 4*d* TMOs have rich phases due to comparable energy scales between electronic correlations such as *U*, *J*, and SOC. Particularly, perovskite ruthenates have recieved considerable attention due to a variety of physical properties including unconventional superconductivity[12], itinerant ferromagnetism[13], and non-Fermi liquid behavior. Extensive studies on are still ongoing to unveil the correlated phases.

The non-Fermi liquid behavior in perovskite ruthenates have been theoretically investigated by studying the Janus effect of *J*. *J* makes the phase far from Mott states, but lowers the quaziparticle weight except for half-filled system[14]. In the region with low quaziparticle but not Mott insulator, it is called as Hund's metal. To show this with experiment, we can use a competitive effect of "*J* vs. cyrstal field"[3]. The key role of *J* is that it equalizes orbital occupancies. On the other hand, crystal field makes different orbital occupancies, making more electrons populate in the lowest-lying orbitals.

The magnetic ordering and its relation to electronic structures in $SrRuO_3$ (SRO) have been also attracted tremendous attentions. The ferromagnetic ordering in SRO breaks time-reversal symmetry, and it gives non-zero Berry curvatures in electronic structures[15]. Anomalous Halle effect (AHE) can detect such electronic structures near Fermi level. According to dimensionality or changes in lattice, the nodal lines and quadratic band crossings near Fermi level can be differed[16]. Therefore, SRO can be good system for studying the relation between topological electronic structures and ferromagnetic ordering.

Especially, there have been a lot of investigations on AHE in ultrathin SRO films. Depending on the film thickness, temperature, and structure, there is a sign reversal or 'hump' anomaly in AHE[17]. It can be induced by real-space magnetic topological features called 'skymions', or can be interpreted by two-channel AHE. Further studies are required on how the magnetic domain in real space affects the transport effect.

1.4 Outline of Thesis

In this dissertation, our goal is to demonstrate hetero-interfacial effects on ultrathin SRO films regarding its electronic correlations and magnetic properties. The main experimental methods will be explained including pulsed laser deposition (PLD), angle-resolved photoemission spectroscopy (ARPES), and magnetotransport in **chapter 2.** In **chapter 3**, we show a phase transition with orbital differentiation. We use strain engineering to SRO monolayer for lifting orbital degeneracy. In **chapter 4**, we demonstrate how the phase of SRO with oxygen vacancy (V_O) is stabilized by hetero-interfacial engineering. The V_O migration at the heterointerfaces successfully induces and controls the amount of V_O. The related magnetic properties will be also discussed. In **chapter 5**, we demonstrate control of two different magnetic phases in SRO films by using hetero-interfacial engineering. We interpret 'hump anomaly' in AHE with multiple AHE loops, suggesting the relation between magnetic domains and AHE.

References

1. Martins, C., Aichhorn, M. & Biermann, S. Coulomb correlations in 4d and 5d oxides from first principles - Or how spin-orbit materials choose their effective orbital degeneracies. *J. Phys. Condens. Matter* **29**, (2017).

2. George, A., Kotliar, G., Krauth, W. & Rozenberg, M. J. Dynamical mean-field theory of strongly correlated fermion systems and the limit of infinite dimensions. *J. Mol. Neurosci.* **35**, 91–100 (2008).

3. Georges, A., De Medici, L. & Mravlje, J. Strong correlations from hund's coupling. *Annu. Rev. Condens. Matter Phys.* **4**, 137–178 (2013).

4. Hwang, H. Y. *et al.* Emergent phenomena at oxide interfaces. *Nat. Mater.* **11**, 103–113 (2012).

5. Dagotto, E. When oxides meet face to face. *Science (80-.).* **318**, 1076–1077 (2007).

6. Kim, T. H. *et al.* Polar metals by geometric design. *Nature* **533**, 68–72 (2016).

7. Kim, J. R. *et al.* Stabilizing hidden room-temperature ferroelectricity via a metastable atomic distortion pattern. *Nat. Commun.* **11**, 1–9 (2020).

8. Ohtomo, A. & Hwang, H. Y. A high-mobility electron gas at the LaAlO3/SrTiO3 heterointerface. *Nature* **427**, 423–427 (2004).

9. Bhattacharya, A. & May, S. J. Magnetic oxide heterostructures. *Annu. Rev. Mater. Res.* **44**, 65–90 (2014).

10. Rondinelli, J. M., May, S. J. & Freeland, J. W. Control of octahedral connectivity in perovskite oxide heterostructures: An emerging route to multifunctional materials discovery. *MRS Bull.* **37**, 261–270 (2012).

11. Majumdar, S. & Dijken, S. Van. Pulsed laser deposition of La1-xSrxMnO3: Thin-film properties and spintronic applications. *J. Phys. D. Appl. Phys.* **47**, (2014).

12. Maeno, Y. *et al.* Superconductivity in a layered perovskite without copper. *Nature* vol. 372 532–534 (1994).

13. Koster, G. *et al.* Structure, physical properties, and applications of SrRuO3 thin films. *Rev. Mod. Phys.* **84**, 253–298 (2012).

14. De'Medici, L., Mravlje, J. & Georges, A. Janus-Faced Influence of Hund's Rule Coupling in Strongly Correlated Materials. *Phys. Rev. Lett.* **107**, 256401 (2011).

15. Fang, Z. *et al.* The anomalous Hall effect and magnetic monopoles in momentum space. *Science (80-.).* **302**, 92–95 (2003).

16. Sohn, B. *et al.* Sign-tunable anomalous Hall effect induced by two-dimensional symmetry-protected nodal structures in ferromagnetic perovskite thin films. *Nat. Mater.* **20**, 1643–1649 (2021).

17. Kimbell, G., Kim, C., Wu, W., Cuoco, M. & Robinson, J. W. A. Challenges in identifying chiral spin textures via the topological Hall effect. *Commun. Mater.* **3**, (2022).

Chapter 2

Experimental Methods

In this chapter, we discuss the experimental methods used for this study. We introduce pulsed laser deposition, which is utilized for fabricating thin films. Measurements of transport and magnetization are introduced. Then, we explain angle-resolved photoemission spectroscopy and spectroscopic ellipsometry.

2.1 Pulsed laser deposition

For deposition of high-quality oxide heterostructures, pulsed laser deposition (PLD) system have been widely used for decades[1]. A pulsed laser ablates a single or poly crystalline target, and the ions coming from the target form plume. Then the ions reach the surface of substrate, and they can be crystallized, forming epitaxial phase.

For this study, we used PLD for the fabrication of epitaxial films. The base pressure of the PLD system (PASCAL co., Japan; Base pressure) was around 10^{-8} Torr. We used a KrF excimer laser (COHERENT, USA; λ = 248 nm). The spot size of the laser on the target surface was modulated using the combination of laser optics. During the growth, the substrate was annealed by a halogen heater. The temperature of the substrate is controlled by manipulating the current supplied to the halogen heater.

For fabricating high quality of the thin films, we need to first prepare atomically flat and single-terminated substrates. For example, $SrTiO_3$ (001) substrate (Crystec) was etched by buffered oxide etch (10:1) for 30 seconds and rinsed by DI water. Then the substrate was annealed at 1000 °C in the atmosphere for 3 hours. If the surface of the treated substrate does not show sharp step terraces, sonicating the substrate with DI water for 1~2 hour will help to achieve Ti-terminated surface. Scandate substrates such as $GdScO_3$ (110), $PrScO_3$ (110), or $DyScO_3$ (110) (Crystec) substrates were etched with DI water for 1-2 hours, and then annealed at 1000 °C in the atmosphere for 3 hours.

We optimized several growth parameters of PLD such as growth pressure (we used

oxygen and argon), substrate temperature, and laser fluence. The growth pressure usually determines stoichiometry of films. Depending on the weight of ions, the amount of scattering can be determined. Then the stoichiometry of ions reaching on the surface of the substrates can be differed. The substrate temperature should be important for crystallizing phases. With *in-situ* reflection high-energy electron diffraction (RHEED), we monitored the electron diffraction intensity from the surface of the films during the deposition. By analyzing the RHEED intensity oscillation, atomic-scale thickness could be controlled (**Fig. 2-1**).

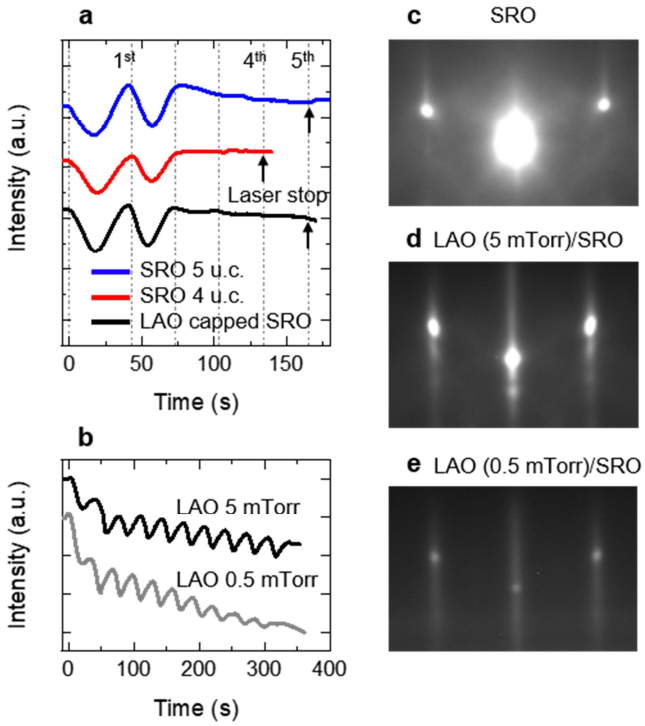

Fig. 2-1. a The intensity of reflection high energy electron diffraction (RHEED) during $SrRuO_3$ (SRO) growth. During the first- and second-layer, it shows layer-by-layer growth. After that, it shows step flow growth. For precise thickness control, the total pulse number is calculated based on the first and second oscillation. **b** Intensity of RHEED during $LaAlO_3$ (LAO) growth, showing layer-by-layer growth mode. **c-e** RHEED patterns after growth of SRO (**c**), LAO (5 mTorr)/SRO (**d**), and LAO (0.5 mTorr)/SRO (**e**) on $SrTiO_3$(001; STO) substrate. Adapted from [2].

In this study, $SrTiO_3$, $SrRuO_3$ and $LaAlO_3$ epitaxial layers were grown on various substrates via PLD. The targets were single-crystalline $SrTiO_3$ and $LaAlO_3$ and polycrystalline $SrRuO_3$. A KrF excimer laser was operated with a repetition frequency of 2 Hz. For deposition of the $SrTiO_3$ and $LaAlO_3$ layers, the laser energy was 1.0 J cm^{-2}, r while that of $SrRuO_3$ was 2.0 J cm^{-2}. The deposition temperature was 700°C for $SrTiO_3$ and $SrRuO_3$, and that of $LaAlO_3$ was 780°C. The oxygen pressure for $SrRuO_3$ was 100 mTorr.

2.2 Transport measurements

Temperature-dependent resistivity and resistivity with external magnetic can imply important physical information of materials[3]. For example, temperature-dependent resistivity can show whether the sample exhibit insulating, Fermi liquid or non-Fermi liquid behavior. Furthermore, anomalous Hall conductivity can imply Berry curvatures near the Fermi level[4].

For such transport measurement, we fabricated Hall bar device on the thin films. To avoid the contact resistance effect, the Hall bar was designed for 4-probe geometry (**Fig. 2-2**). Ultraviolet photolithography and Ar ion milling system were used. We used AZ5214E as a photoresist. Then 20 nm of Au layer was deposited with electron beam evaporation. We used Physical Properties Measurement System (PPMS, Quantum Design).

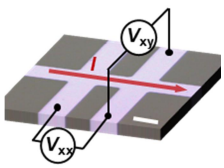

Fig. 2-2. Optical microscopic image of 50×50 μm^2 Hall bar. The scale bar indicates 50 μm. Adapted from [2].

The Hall effect is the generation of a voltage difference that is transverse to the

applied current and perpendicular to the applied magnetic field. When charge carriers, such as electrons or holes, moves with external magnetic field, they can experience the Lorentz force as follows.

$$\boldsymbol{F} = q(\boldsymbol{E} + \boldsymbol{v} \times \boldsymbol{B})$$

Here, $\boldsymbol{v}$ is the velocity of the charge, $\boldsymbol{E}$ is applied electric field, and $\boldsymbol{B}$ is applied external field. For steady states ($\boldsymbol{F}$ = 0), the voltage difference along *y* direction can be induced in geometry as **Figure 2-2**, when the external field is applied as out-of-plane. This is called 'ordinary Hall effect (OHE)', and it is proportional to external magnetic field. From extracting the slope of OHE, we can obtain the type of charge carrier and their carrier density.

With time-reversal symmetry breaking, such as ferromagnetic systems, the anomalous Hall effect (OHE) can be induced due to non-zero Berry curvature. Therefore, the Hall resistivity (ρ_{xy}) can be described by $\rho_{xy} = \rho_{OHE} + \rho_{AHE}$. Here, ρ_{OHE} can be expressed as $\rho_{OHE} = R_0 H$, where R_0 is the ordinary Hall coefficient and *H* is the perpendicular magnetic field. Since we are interested in AHE, we subtracted the ρ_{OHE} component by linear fitting the ρ_{xy}–*H* curves (**Fig. 2-3**).

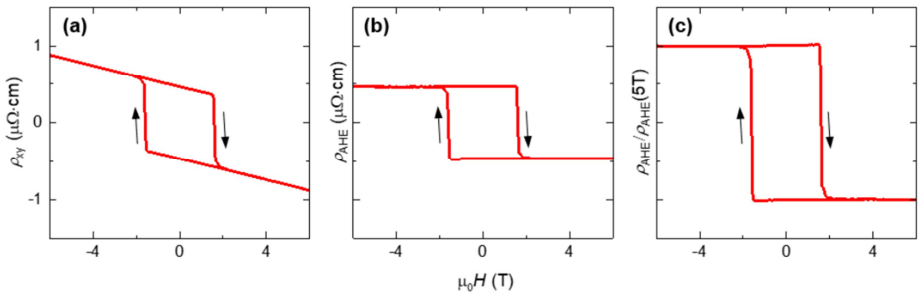

Fig. 2-3. We extracted the OHE part by linear fitting. Adapted from [5].

2.3 Magnetization measurements

For measuring magnetic properties of films, we used a Magnetic Properties Measurement System (MPMS, Quantum Design). The temperature dependent magnetization was measured in vibrating-sample magnetometry (vsm) using superconducting quantum interference device (SQUID). We polished the backside of samples to remove the possible magnetic signal from pt paste used during PLD.

2.4 Angle-resolved photoemission spectroscopy

Angle-resolved photoemission spectroscopy (ARPES) technique is based on the photoelectric effect, where a photon ejects an electron from a material. During the ARPES measurement, the photon energy ejects the electrons in the sample into the vacuum, following below equation. E_k is the kinetic energy of emitted electrons, hv is photon energy, E_B is binding energy of the sample, and Φ is work function.

$$E_k = hv + E_B + \Phi$$

By analyzing E_k and angles (θ, φ) of the emitted electrons, it can probe the momentum resolved band structures (**Fig. 2-4**). The momentum ($\boldsymbol{p}$) which is parallel to the surface ($\boldsymbol{p}_{||}$) is conserved, and it follows equation as below. On the other hand, $\boldsymbol{p}$ perpendicular to the surface ($\boldsymbol{p}_{\perp}$) is not conserved since it experience surface.

$$|\boldsymbol{k}_{||}| = \frac{2\pi}{h}\sqrt{2m_e(E_k)}\sin\theta$$

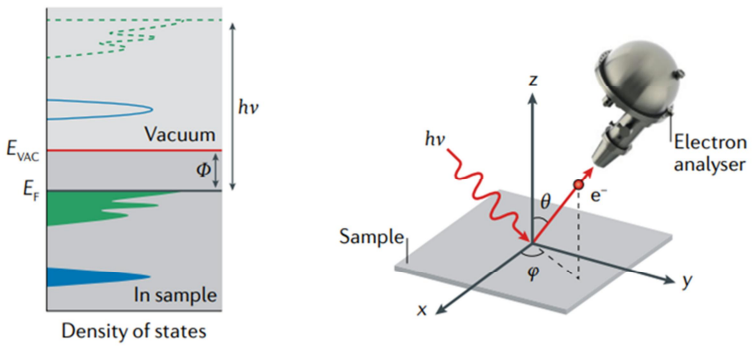

Fig. 2-4. ARPES technique. When electron absorb photon, it is emitted into vacuum. By analyzing the emitted angles, angle-resolved momentum in the *x* and *y* directions can be collected. Adopted from [6].

After PLD growth, the oxide heterostructures were transferred in a ultra-high vacuum (< 1.0 E-10 Torr) without air exposure. *in-situ* ARPES measurements were performed using home lab equipment consists of an analyzer (DA30; Scienta) and discharge lamp (the Fermi instrument). An He-Iα ($h\nu$ = 21.2 eV) light was used. To avoid charging problem, we inserted an electron-absorbing layer between the substrate and 10 u.c $SrTiO_3$ layer. The $SrTiO_3$ layer decouples the electronic structure of the topmost layer from that of the inserted conducting layer.

2.5 Spectroscopic ellipsometry

Optical spectroscopy is a powerful tool for investigating electronic structures in TMOs. By analyzing the light-matter interactions, intraband (free carrier excitation) or interband transitions (between valence and conduction bands) can be detected. We perform optical spectroscopic characterization of thin films by using a spectroscopic ellipsometer (M-2000 DI; J.A. Woollam Co.). In this section we introduce details on spectroscopic ellipsometry.

When *p*- or *s*- polarized light reaches to the interface, entering medium N_1 from medium N_0, it is reflected, or transmitted. The Φ_0 and Φ_1 are angles of incident and refracted light. The Fresnel's reflection equations are as below. Here, it follows the Snell's law ($N_0 \sin\Phi_0 = N_1 \sin\Phi_1$).

$$r_p = \frac{E_{rp}}{E_{ip}} = \frac{N_1 \cos\Phi_0 - N_0 \cos\Phi_1}{N_1 \cos\Phi_0 + N_0 \cos\Phi_1}$$

$$r_s = \frac{E_{rs}}{E_{is}} = \frac{N_0 \cos\Phi_0 - N_1 \cos\Phi_1}{N_0 \cos\Phi_0 + N_1 \cos\Phi_1}$$

The ellipsometry measures the reflection of both *p*- and *s*- polarized lights and obtains the intensity ratio (ψ) and rotated angle of polarization between the two (Δ). From experimental variables, the real and imaginary part of dielectric constants can be obtained.

$$\rho = \frac{r_p}{r_s} = \tan\psi\, e^{i\Delta} \text{ , where } \psi = \frac{|r_p|}{|r_s|} \text{ and } \Delta = \varphi_p - \varphi_s$$

Near infrared region, the motion for the free carriers can be analyzed by Drude model. Near visible or ultraviolet region, there can be interband transitions: from occupied state to unoccupied state. Also, due to orbital hybridization, inter-atomic optical transitions can be detected by spectroscopic ellipsometer. By analyzing position and intensity of peaks, we can investigate electronic structures of TMOs.

References

1. Blank, D. H. A., Dekkers, M. & Rijnders, G. Pulsed laser deposition in Twente: From research tool towards industrial deposition. *J. Phys. D. Appl. Phys.* **47**, (2014).

2. Ko, E. K. *et al.* Tunable Two-Channel Magnetotransport in SrRuO3 Ultrathin Films Achieved by Controlling the Kinetics of Heterostructure Deposition. *Adv. Electron. Mater.* **8**, 1–8 (2022).

3. Masatoshi, I., Atsushi, F. & Yoshinori, T. Metal-insulator transition. *Rev. Mod. Phys.* **70**, 1039 (1998).

4. Fang, Z. *et al.* The anomalous Hall effect and magnetic monopoles in momentum space. *Science (80-.).* **302**, 92–95 (2003).

5. Ko, E. K. *et al.* Oxygen Vacancy Engineering for Highly Tunable Ferromagnetic Properties: A Case of SrRuO3 Ultrathin Film with a SrTiO3 Capping Layer. *Adv. Funct. Mater.* **30**, 2001486 (2020).

6. Yang, H. *et al.* Visualizing electronic structures of quantum materials by angle-resolved photoemission spectroscopy. *Nat. Rev. Mater.* **3**, 341–353 (2018).

7. Theeten, J. B. & Aspnes, D. E. Ellipsometry in thin film analysis. *Annu. Rev. Mater. Sci.* **11**, 97–122 (1981).

Chapter 3

Orbital-selective phase transition in a two-dimensional correlated system

Hund's rule coupling (J) has recently attracted much attention to describe the novel quantum phases of multi-orbital materials. However, their experimental confirmations have been difficult due to complications in controlling effective quantum parameters such as orbital degeneracy. Here, we demonstrate the method to systematically investigate the role of J in the Hund's correlated system. By growing $SrRuO_3$ monolayers on various substrates with symmetry-preserving interlayers, we gradually tuned the orbital degeneracy in the two-dimensional (2D) ruthenates. This effectively tunes the orbital occupancy through the 2D quantum confinement effect. Using in situ angle-resolved photoemission spectroscopy, we observed a progressive metal-insulator transition, which occurs with orbital differentiation. The MIT corresponds to the concurrent opening of a band insulating gap in d_{xy} orbital and a Mott gap in $d_{xz/yz}$ orbital. Our study provides an effective experimental approach for searching the multi-orbital physics.

3.1 Introduction

3.1.1 Hund's rule coupling in perovskites

To understand physical properties of materials with partially filled *d*- or *f*-orbitals, electronic correlations should be considered. For example, Mott insulating states can be well described by strong on-site Coulomb repulsion (U), and it has been a central paradigm in physics since the 1940s[1]. Recently, Hund's rule coupling (J) has been extensively investigated theoretically for describing unconventional quantum phases in multi-orbital systems[2–11], such as 3*d* iron-based superconductors, 4*d* ruthenates, and recently discovered Ni-based superconductors. Considering J, several new concepts, including spin-freezing[11], and spin-orbital separation (SOS)[8] have been proposed.

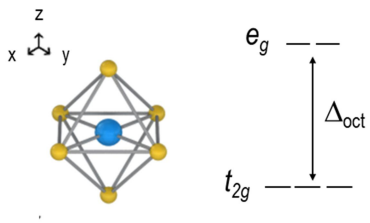

Fig. 3-1 Crystal field splitting of *d*-orbitals due to oxygen octahedron in perovskites.

In perovskite oxides (ABO_3), the BO_6 octahedron gives a crystal field splitting among five *d* orbitals. This will break the original degeneracy of the *d* orbitals into three t_{2g} orbitals and two e_g orbitals (**Fig. 3-1**). Interestingly, when we consider the three t_{2g} orbitals, the role played by *J* in the energetics of the Mott gap is ambivalent according to dynamical mean-field theory (DMFT) calculations (**Fig. 3-2**). It strongly depends on the number of electrons. For example, the critical *U* value required for the Mott transition is smaller for half-filled system compared to non-half-filled system.

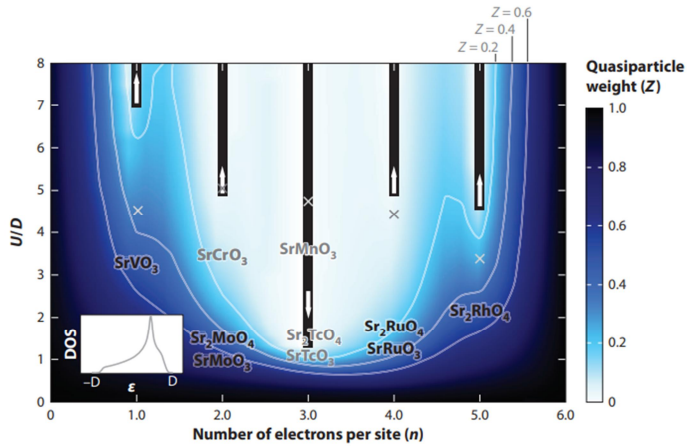

Fig. 3-2. Map for degree of correlations for partially occupied three t_{2g} orbitals. The white arrow indicates direction of increasing *J*. The black bar indicates Mott state. For 3-orbital/3-electron system (half-filled), *J* helps to open the Mott gap. Adapted from [2].

Despite the intriguing property of J, experimental investigation on J is challenging. First, it is difficult to control U or J values in real materials since these are already determined by atomic physics. Second, systematic investigation with control of the orbital occupancy is challenging without the modification of the crystal structure or chemically doping systems.

3.1.2 Symmetry-preserving strain engineering of $SrRuO_3$ monolayer

To explore Hund's physics, a novel technique called symmetry-preserving strain engineering has been investigated. Epitaxial strain has been applied on $SrRuO_3$ (SRO) monolayers by using various substrates, which have different in-plane lattice parameters. However, when we are applying epitaxial strains using different substrates, we should consider its structural proximity effects too. Structural symmetry of ultrathin films usually follows that of the substrate. Note that the bulk SRO is orthorhombic structure with oxygen octahedral distortions. Its oxygen octahedral rotation (OOR) patterns in the Glazer notation is $a^-b^+c^-$. (*a*, *b*, and *c* are pseudocubic axis direction). Since we only wanted changes in in-plane lattice constants, we inserted a symmetry-preserving buffer layer: the $SrTiO_3$ (STO) layer between the SRO layer and substrate. It made the structural symmetry of SRO monolayer preserved while having different epitaxial strains.

The symmetry-preserving epitaxial strain on SRO monolayers can give a tetragonal distortion by varying *c*/*a* (**Fig. 3-3**). The originally degenerate three t_{2g} orbitals will become lifted. For example, tensile strain makes $c/a < 1$ and the energy level of d_{xy} orbital will be lowered compared to that of the $d_{xz/yz}$ orbitals. We call this splitting as a tetragonal crystal field splitting (Δ_t). Control of Δ_t will redistribute electrons in the t_{2g} orbitals. Note that bulk SRO is metallic state and has 3 t_{2g} orbitals with 4 electrons (hereafter, 3-orbital/4-electron). When the tensile strain gives larger Δ_t, the energy level of d_{xy} will go down away from the Fermi energy (E_F) and then 2 electrons will be fully filled.

Since the other 2 electrons will be redistributed in the $d_{xz/yz}$ orbitals, the system will be half-filled. In this half-filled system, Mott transition can be happened with help of J. Note that this electronic structural change can be enhanced in the two-dimensional (2D) system due to quantum confinement effect.

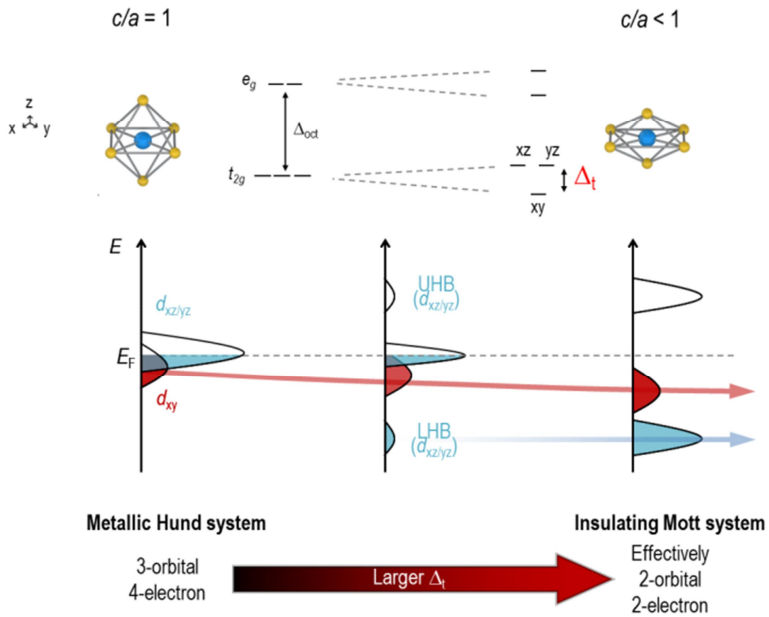

Fig. 3-3. Symmetry-preserving strain engineering on SRO monolayer.

3.2 Structural characterization

SRO monolayers were deposited on $(LaAlO_3)_{0.3}(Sr_2TaAlO_6)_{0.7}$(001) [LSAT(001)], $SrTiO_3$(001) [STO(001)], $Sr_2(Al,Ga)TaO_6$(001) [SAGT(001)], $KTaO_3$(001) [KTO(001)], and $PrScO_3$(110) [PSO(110)]. The substrates impart −1.4%, −0.5%, +0.2%, +1.7%, and +2.5% epitaxial strain to the SRO monolayers. Compressive (tensile) strain is indicated as a minus (plus) sign. The symmetry-preserving buffer layer (a 10-unit-cell (u.c.) STO) buffer layer was also deposited.

Fig. 3-4 shows structural information of SRO monolayers. By inserting the STO buffer layer, we confirmed the SRO monolayer with the $a^0a^0c^-$ symmetry independent of substrates. Scanning transmission electron microscopy (STEM) images of SRO monolayers shows abrupt interfaces. To protect the topmost layer (SRO monolayer) during the STEM measurements, a 10-u.c. STO capping layer was deposited. As shown in the image, there were no in-plane OOR angles in SRO. Note that there were a few regions with thickness inhomogeneity (zero or two Ru-layers). These regions hinder transport measurements, giving discontinuities in the electronic path.

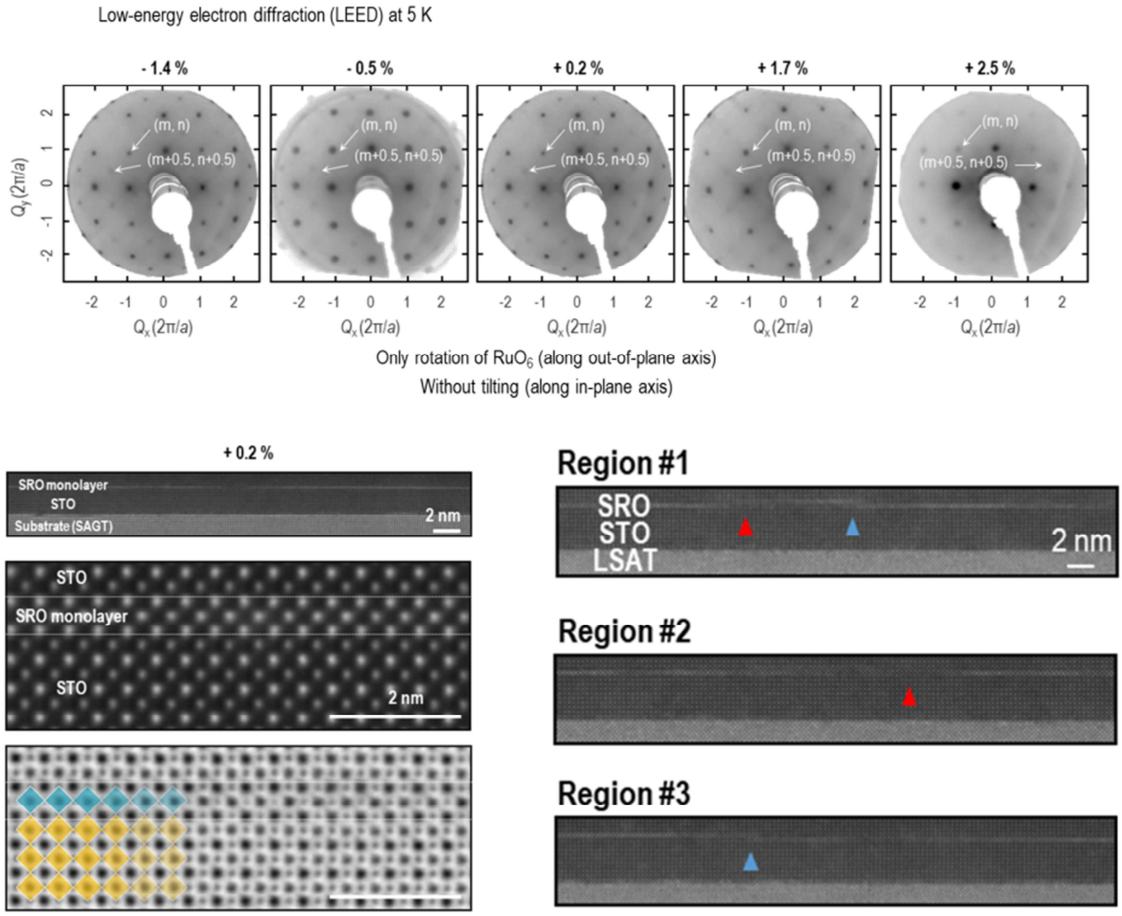

Fig. 3-4. Structural characterization for SRO heterostructures. Low-energy electron diffraction patterns for SRO monolayers shows symmetry-preserving strain engineering were successful. STEM images indicate high-quality of SRO single layer. Occasionally, we observed small regions with thickness inhomogeneity.

3.3 Control of the electronic structure of the $SrRuO_3$ monolayers

We confirmed that SRO monolayer with -1.4% of strain is a two-dimensional (2D) metal by measuring *in-situ* ARPES (**Fig. 3-5**). Since the SRO monolayer is 2D system, its electronic structure should be similar to that of Sr_2RuO_4. Sr_2RuO_4 is a well-established quasi-2D system. The Fermi surface (FS) of monolayer SRO (−1.4%) was similar to the schematic FS of Sr_2RuO_4. There are the three bands at E_F and they are labeled as α, β, and γ. The α and β bands are dominantly given by $d_{xz/yz}$ orbitals, and of γ is given by d_{xy} orbital.

With symmetry-preserving strain engineering, the electronic structure of the SRO monolayer could be controlled systematically. While compressively strained monolayers (−1.4 and −0.5%) had a nonzero density of states (DOS) at E_F, the SRO monolayers under a tensile strain of +0.2% was insulating. Therefore, there should be the metal-to-insulator transition (MIT) around +0.2% of strain. To understand the MIT, we measured strain-dependent *E-k* dispersion along the Γ-M line. There were two major changes with more tensile strain. Firstly, the position of a band near M/2 (red line) moved to higher binding energies. Secondly, there was a sudden enhancement of the spectral weight (*SW*) near Γ (blue line) at a tensile strain of +0.2%.

We found that the band near M/2 (Γ) guided by the red (blue) line should have a dominant d_{xy} ($d_{xz/yz}$) orbital character according to ARPES measurements with various experimental geometries (**Fig. 3-6**). This is consistent with the schematic in **Fig. 3-3**. As more tensile strain applied, the d_{xy} (near M/2) moved downward and became fully-filled at the MIT. The $d_{xz/yz}$ (near Γ) appeared close to the MIT and it should be lower Hubbard bands (LHBs).

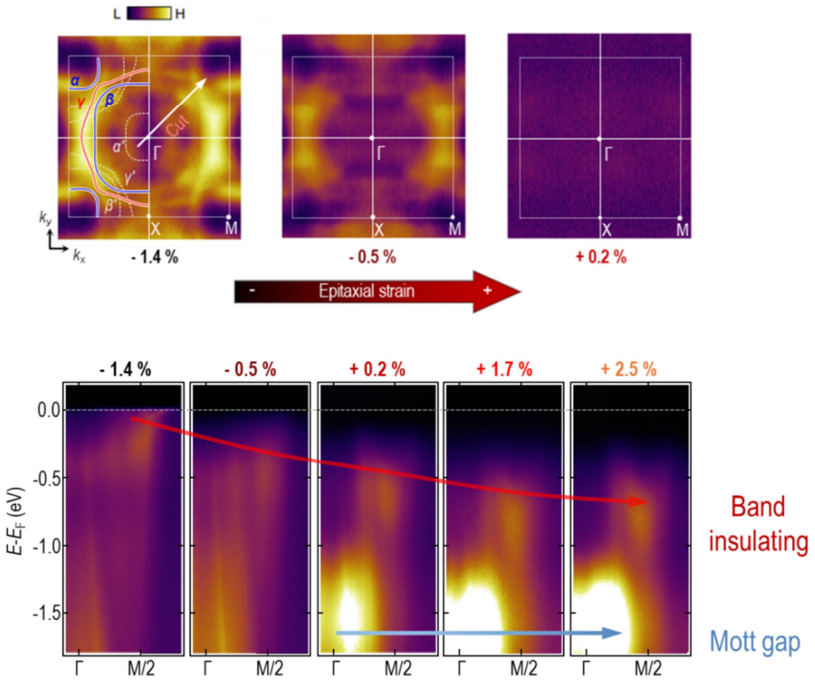

Fig. 3-5. Metal-to-insulator transition induced by epitaxial strain in SRO monolayers.

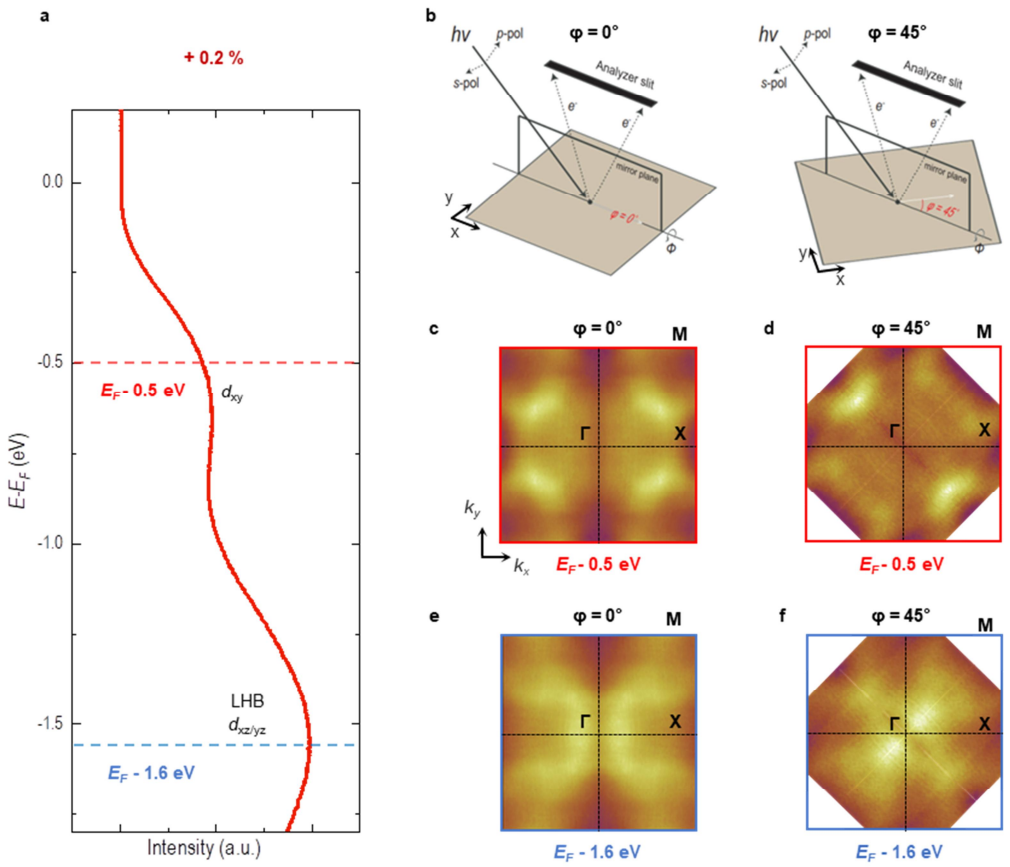

Fig. 3-6. Orbital contributions of the incoherent bands below the Fermi energy (E_F) in an SRO monolayer under +0.2% strain. a, Energy distribution curve (EDC) of the SRO monolayer (+0.2%) along the Γ-M line. To explore the orbital character, we measured the constant-energy map at various azimuthal angles (φ). The maps were obtained at $E_F - 0.5$ eV (red dashed line) and $E_F - 1.6$ eV (blue dashed line) using dominantly s polarized light. b, experimental geometry for $\varphi = 0°$ and 45°. c, d, Energy-constant maps at $E_F - 0.5$ eV with $\varphi = 0°$ (c) and 45° (d). e, f, Energy-constant map at E_F –1.6 eV with $\varphi = 0°$ (e) and 45° (f).

3.4 Interatomic optical transitions and filling control

To investigate the electron filling among orbitals, we observed the interatomic optical transitions between Ru^{4+} ions (**Fig. 3-7**). There can be electron hopping from one Ru ion to another Ru ion when the electron absorbs a photon. This is called *d-d* transition ($d^4 + d^4 \rightarrow d^3 + d^5$ transition). There can be large interatomic transition peak between the same orbitals due to orbital hybridization (Ru *d* – O *p*). In other words, there can be interatomic transition from d_{xy} to d_{xy} (or from d_{xz} to d_{xz}) considering matrix element. In multi orbital system, *J* plays an important role in electron hopping. Considering matrix elements and *U, J* values, a (3-orbital/4-electron) material can have two interatomic transitions ($U - J$ and $U + J$). On the other hand, when d_{xy} become fully-filled due to large tensile strain [(2-orbital/2-electron) system], the $U - J$ transition disappears.

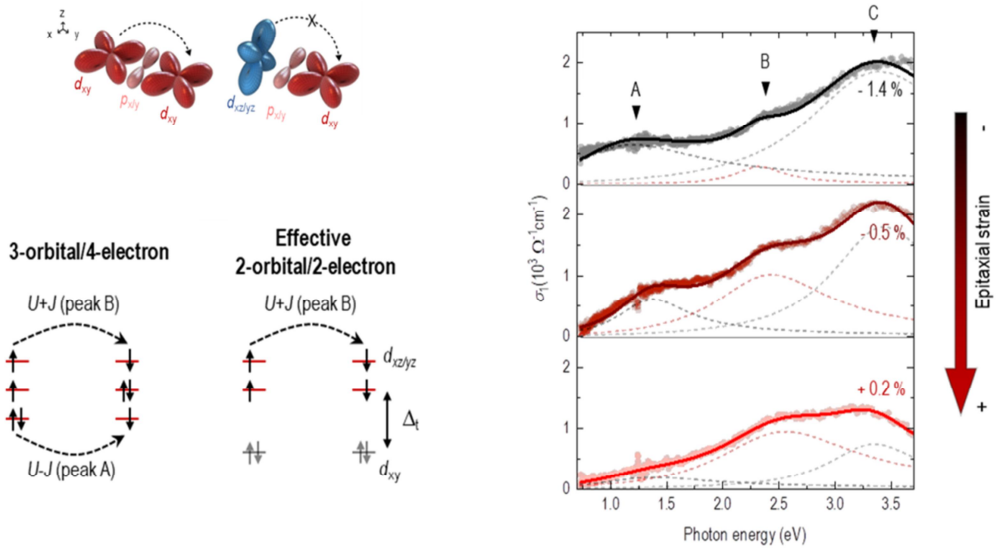

Fig. 3-7. Interatomic optical transitions in SRO and optical spectra obtained by spectroscopic ellipsometry.

We obtained an optical spectra via spectroscopic ellipsometry for SRO monolayers with -1.4%, -0.5%, and +0.2% of strains. By fitting the spectra (solid circles) with Lorentzian oscillators (dashed lines), we found that there were three peaks A, B, and C. Peak C is charge transfer peak from O 2*p* to Ru t_{2g}. The A and B peaks are due to *d*-*d* transition. They are with energy positions at $U - J$ and $U + J$, respectively. Note that the peak positions are well matched with previous reports of bulk ruthenates[13]. With tensile strain, peak A become disappeared. It indicates that the tensile strain change the system from (3-orbtial/4-electron) to (2-orbital/2-electron) system. From analyzing the peak positions, we could extract J value ~0.6 eV[13].

3.5 Conclusion

We investigated Hund's physics in 2D oxides. By controlling the tetragonal crystal field splitting, we could redistribute electron fillings. Symmety-preserving strain engineering of SRO monolayers induced MIT. Moreover, we confirmed that the SRO monolayer could be vary between (3-orbital/4-electron) and (2-orbital/2-electron) systems. The results confirmed that J made the half-filled system easier to open Mott gap, which is consistent to the ambivalent nature of J expected in theoretical works. Moreover, the symmetry-preserving strain engineering technique can be widely used to other 3*d*, 4*d*, and 5*d* transition metal oxides. Control of the number of orbitals/electrons will be useful for exploring orbital-selective physics in multi-orbital systems.

References

1. Mott, N. F. The basis of the electron theory of metals, with special reference to the transition metals. *Proc. Phys. Soc. Sect. A* **62**, 416–422 (1949).

2. Georges, A., De Medici, L. & Mravlje, J. Strong correlations from hund's coupling. *Annu. Rev. Condens. Matter Phys.* **4**, 137–178 (2013).

3. Hirjibehedin, C. F. Magnetic atoms: The makings of a Hund's metal. *Nat. Nanotechnol.* **10**, 914–915 (2015).

4. Mravlje, J. *et al.* Coherence-incoherence crossover and the mass-renormalization puzzles in Sr2RuO4. *Phys. Rev. Lett.* **106**, 096401 (2011).

5. Kugler, F. B. *et al.* Strongly Correlated Materials from a Numerical Renormalization Group Perspective: How the Fermi-Liquid State of Sr2RuO4 Emerges. *Phys. Rev. Lett.* **124**, 16401 (2020).

6. Deng, X. *et al.* Signatures of Mottness and Hundness in archetypal correlated metals. *Nat. Commun.* **10**, 2721 (2019).

7. Stadler, K. M., Kotliar, G., Lee, S. S. B., Weichselbaum, A. & Von Delft, J. Differentiating Hund from Mott physics in a three-band Hubbard-Hund model: Temperature dependence of spectral, transport, and thermodynamic properties. *Phys. Rev. B* **104**, 115107 (2021).

8. Stadler, K. M., Kotliar, G., Weichselbaum, A. & von Delft, J. Hundness versus Mottness in a three-band Hubbard–Hund model: On the origin of strong correlations in Hund metals. *Ann. Phys. (N. Y).* **405**, 365–409 (2019).

9. Ryee, S., Han, M. J. & Choi, S. Hund Physics Landscape of Two-Orbital Systems. *Phys. Rev. Lett.* **126**, 206401 (2021).

10. De'Medici, L., Mravlje, J. & Georges, A. Janus-Faced Influence of Hund's Rule Coupling in Strongly Correlated Materials. *Phys. Rev. Lett.* **107**, 256401 (2011).

11. Werner, P., Gull, E., Troyer, M. & Millis, A. J. Spin freezing transition and non-fermi-liquid self-energy in a three-orbital model. *Phys. Rev. Lett.* **101**, 166405 (2008).

12. Rondinelli, J. M., May, S. J. & Freeland, J. W. Control of octahedral connectivity in perovskite oxide heterostructures: An emerging route to multifunctional materials discovery. *MRS Bull.* **37**, 261–270 (2012).

13. Lee, J. S. *et al.* Electron and Orbital Correlations in Ca2-xSrxRuO4 Probed by Optical Spectroscopy. *Phys. Rev. Lett.* **89**, 257402 (2002).

Chapter 4

Heteros-interfacial control for oxygen vacancy migration

In this chapter, we demonstrate how the phase of $SrRuO_3$ (SRO) with oxygen vacancy (V_O) is stabilized by utilizing hetero-interfacial engineering. The high kinetic process during pulsed laser deposition helps V_O to overcome the migration barrier energy at the heterointerface between $SrTiO_3$ and SRO. Furthermore, we show the systematic control of magnetic coercive field of SRO depending on the amount of V_O.

4.1 Introduction

4.1.1 Oxygen vacancies in transition metal oxides

The well-defined oxide heterointerfaces with functionalities have great potential for device applications. For example, ferromagnetic oxide heteorstructures can be used for spintronics devices if we can control the magnetic properties, such as magnetic switching. Control of oxygen vacancy (V_O) in transition metal oxides (TMO) can be one of the most effective ways for modulation of functional properties. There have been intriguing physical properties such as metal-to-insulator transition, and ferroelectricity with metallicity. When the point defects are ordered in two-dimension, two-dimensional electron liquid state can emerge[1,2]. They can also form nanoscale filaments, which can be used for resistive-switching devices[3,4]. Recently, unconventional superconductivity in infinite nickelate structure has been observed, where the apical oxygen is selectively removed[5].

4.1.2 Oxygen vacancy migration to $SrRuO_3$ ultrathin films

$SrRuO_3$ (SRO) is one of the most widely used electrode layers among TMOs. Due to their electron-electron correlation such as on-site Coulomb interaction and Hund's rule coupling, a variety of intriguing physical properties can be emerged[6]. For example, it exhibits non-Fermi liquid behavior, itinerant ferromagnetism with strong magnetic anisotropy (MA). Note that there are strong coupling between spin, orbital, charge and lattice degrees of freedom. If we can introduce V_O to SRO and control the amount of V_O, we can locally change the structure, orbital occupancy, and spin configuration.

Compared to other TMOs, however, study on V_O in SRO is quite difficult. There are typical ways for generating V_O in oxides: synthesis or post-annealing in reducing environments[7]. First, fabricating oxides with low oxygen partial pressure [$P(O_2)$] can induce V_O. Second, post-annealing at high vacuum or hydrogen gas can increase V_O concentration in oxides. However, these methods cannot induce V_O in SRO films, but induce Ru deficiency. RuO_2 is highly volatile, so Ru vacancy is induces during those processes. Therefore, a new method is required for creating and controlling the V_O in SRO.

4.1.3 Control of kinetic energy of ions during pulsed laser deposition

We suggested control of kinetic energy of ions during pulsed laser deposition can induce V_O migration into SRO films. In $SrTiO_3$/SRO (STO/SRO) ultrathin heterostructures, V_O allows fine control of its ferromagnetic properties, too. **Fig. 4-1** shows our strategy for V_O migration. The V_O formation energy in SRO is smaller than that of STO[8]. However, there is barrier energy (~1 eV) at the heterointerfaces for the V_O migration from STO to SRO. This energy barrier is quite large. It cannot be overcome by the thermal energy of the post-annealing process or by a film growth method with a small kinetic ion energy (such as molecular beam epitaxy).

The high kinetic energy of ions during PLD can help the V_O migrate across the STO/SRO interface. If we deposit the STO capping layer with low growth pressure, the ions can arrives on the surface of SRO with higher kinetic energies. Then the V_O will be able to overcome the barrier energy. Moreover, the V_O concentration will be controlled by varying the thickness or growth pressure of the STO capping layer. Following, we expect V_O can result in significant modulations of the magnetic properties of SRO ultrathin films, further promoting SRO-based heterostructures for practical spintronic/electrical device applications.

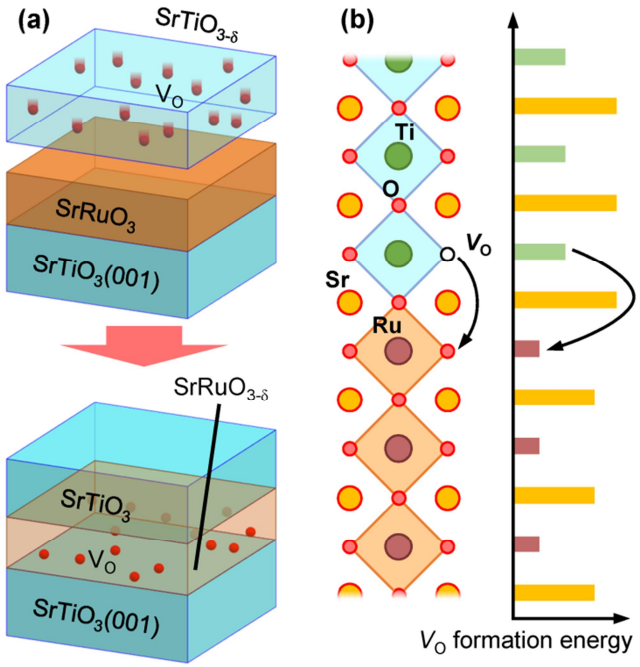

Fig. 4-1. Schematics of oxygen vacancy (V_O) configuration in $SrTiO_3/SrRuO_3/SrTiO_3(001)$ [STO/SRO/STO(001)] heterostructures during pulsed laser deposition (PLD). The red dots in $SrTiO_{3-\delta}$ and $SrRuO_{3-\delta}$ indicate V_O. **a** Oxygen deficient $SrTiO_{3-\delta}$ film was deposited on an SRO film. V_O in the STO capping layer migrates into the SRO layer underneath during deposition, resulting in oxygen deficient $SrRuO_{3-\delta}$. **b** The formation energy of V_O is plotted according to the position of V_O in the STO/SRO heterostructure. The black arrows indicate V_O migration from the capping STO into the underlying SRO. Adapted from [9].

4.2 Oxygen vacancy in $SrRuO_3$

By PLD, we deposited STO/SRO heterostructures on STO(001) substrates. The thickness of SRO (t_{SRO}) was fixed as 5 unit-cells (u.c.) while the thickness of STO (t_{STO}) was varied as 1 to 10 u.c. During the growth of STO capping layers, $P(O_2)_{STO}$ was controlled from 0.01 to 100 mTorr. It is natural that low $P(O_2)_{STO}$ should the V_O concentration of the STO capping layer, rather than that of the underneath SRO layer. However, we found that low $P(O_2)_{STO}$ induces V_O concentration of the SRO films.

To investigate V_O in SRO, we measured scanning transmission electron microscopy (STEM) in annular bright-field (ABF) mode, where the position of oxygen ions can be detected. Image formation by ABF-STEM is very sensitive to light elements. **Fig. 4-2** shows ABF images of two different STO/SRO heterostructures. The thickness of STO capping layers are both 10 u.c., while the $P(O_2)_{STO}$ were 100 and 5 mTorr, respectively. We denoted the samples as STO(100 mTorr)/SRO and STO(5 mTorr)/SRO. With low magnification ABF images, the STO(100 mTorr)/SRO sample shows a uniform atomic contrast in both the SRO and STO regions. On the other hand, that of the STO(5 mTorr)/SRO sample shows some inhomogeneous variations of contrast in SRO layers. Note that STO layers and STO substrates have uniform atomic contrast, maintaining sharp interfaces. The could-like contrast in SRO layers can be caused by dechanneling effects coming from high density of point defects.

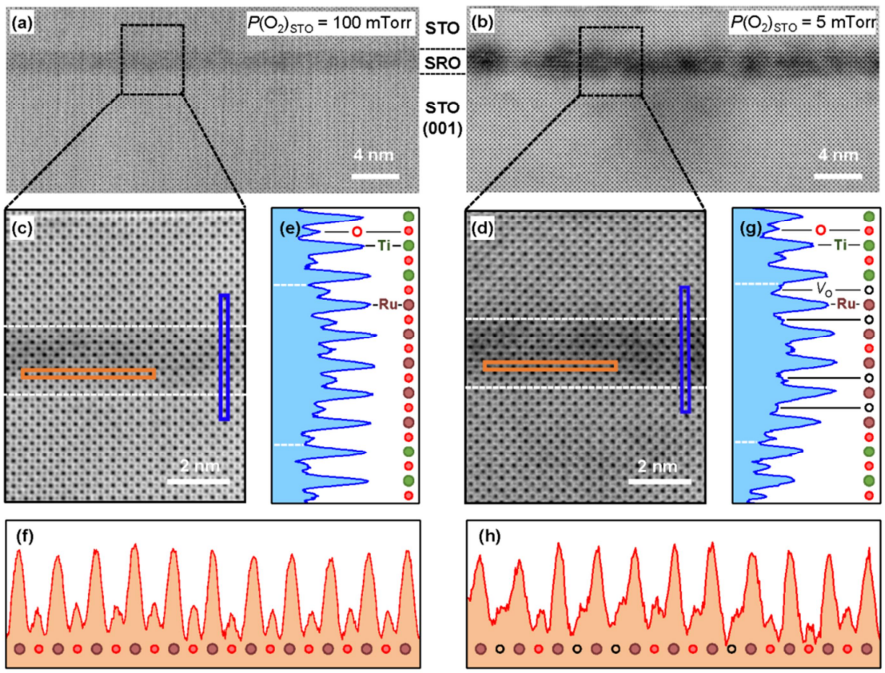

Fig. 4-2. Investigation of V_O in SRO by scanning transmission electron microscopy (STEM). **a, b** Atomically resolved annular bright-field (ABF) images of (**a**) STO/SRO thin films where the oxygen partial pressure during the STO capping layer deposition [$P(O_2)_{STO}$] is 100 mTorr [STO(100 mTorr)/SRO] and (**b**) 5 mTorr [STO(5 mTorr)/SRO]. The SRO layer in (**a**) has uniform intensity contrast whereas (**b**) shows obvious contrast variations, suggesting the existence of defects in STO(5 mTorr)/SRO **c**, **d**) Magnified images of preselected regions in (**a**) and (**b**) (dashed boxes). **e-h**) Inverted intensity line profiles extracted from vertical and horizontal BO_2 (TiO_2 or RuO_2) atomic planes. The

high intensity peaks indicate heavy cations such as Ru (solid brown circles) and Ti (solid green circles). The peaks of much lower intensity indicate oxygen sites (solid red circles). For both samples, the clear peaks of all of the cation and oxygen in STO(001) and STO suggest few cation vacancies and V_O in the substrate and STO layer. In contrast, the intensity of oxygen peaks of SRO fluctuates in STO(5 mTorr)/SRO as shown in (**g**), and (**h**), whereas the oxygen peaks of SRO in STO(100 mTorr)/SRO are still uniform, as indicated in (**e**), and (**f**). The non-uniform and weak intensity of oxygen sites in STO(5 mTorr)/SRO suggest a high-density of V_O (open black circles). Adapted from [9].

Now we focus on analyzing oxygen peaks in ABF images for investigating the nature of these defects. The magnified ABF images shows clear oxygen ion peaks. We plotted line profiles for inverted intensity along TiO_2 and RuO_2 lines. The high-intensity peaks indicate cations (Ti or Ru). The small-intensity peaks represent oxygen ions. In STO capping layers and substrates, all of peaks are well-defined with uniform intensities. On the other hand, the position and intensity of oxygen peaks in the SRO regions of these two samples were different. The oxygen peaks in the SRO region in the STO(100 mTorr)/SRO sample were uniform. For the STO(5 mTorr)/SRO sample, however, the oxygen peak intensities fluctuated and in some regions, peak positions were not well-defined. The oxygen peaks are too weak of smeared by the background at some region. It indicates the high-density V_O. The STEM-ABF results show that V_O can migrate into SRO during STO capping layer deposition and keep the layer from noticeable cation vacancies.

To see the influence of V_O on structural distortion of the SRO layer, we analyzed precise position of cations (**Fig. 4-3**). From the STEM images in high-angle annular dark-field (HAADF) mode, we could extract the ratio between the out-of-plane lattice constant and the in-plane lattice constant (c/a). Our samples were fully-strained and SRO films are compressively strained with 0.5%. According to poisson ratio of bulk SRO, the c/a_{sub} in SRO films should be close to 1.02. For the STO(100 mTorr)/SRO sample, this c/a is close to 102 %. Therefore, the c-lattice expansion should be mainly attributed to the epitaxial strain. However, for the STO(5 mTorr)/SRO sample, there is significantly large c-lattice expansion. The c/a_{sub} values in the SRO region, especially at near the top interface, show

a sizable increase. The maximum c/a_{sub} value reaches 105 %, and such a high c/a_{sub} value can be induced by V_O. According to *c*-lattice expansion, we can conclude that there is higher V_O concentration near interface between top STO and SRO. The different amount of V_O depending on the atomic rows might induce inversion symmetry breaking.

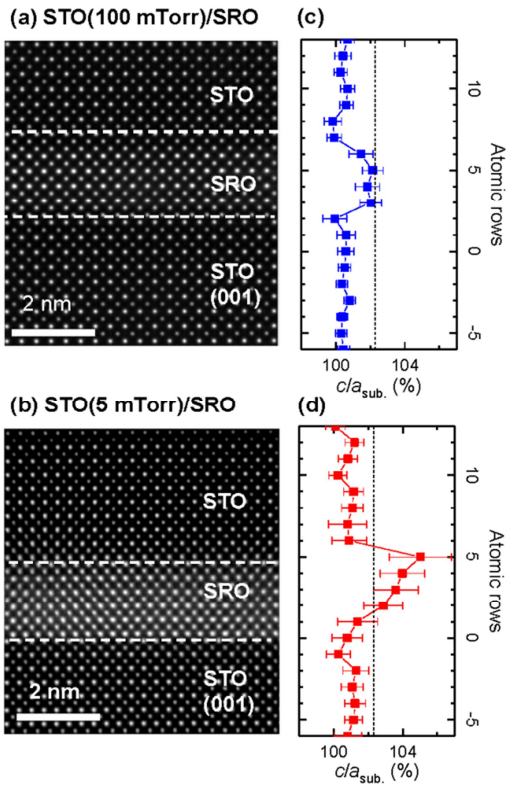

Fig. 4-3. Investigation of structural distortion in SRO by STEM. **a, b** High angle annular dark-field (HAADF) images of (**a**) STO(100 mTorr)/SRO and (**b**) STO(5 mTorr)/SRO. **c, d** Integrated ratio of the *c*-lattice of the bilayers to the in-plane lattice constant of the substrate (c/a_{subs}). Note that the maximum of c/a_{subs} in SRO is 102 % in STO(100 mTorr)/SRO, and 105 % in STO(5 mTorr)/SRO. The predicted c/a_{subs} of compressively-strained SRO thin film on STO(001), according to the Poisson ratio, is denoted by the dashed line in (**c**), (**d**). The significant increase of c/a_{sub} in STO(5 mTorr)/SRO compared

to STO(100 mTorr)/SRO suggests that high V_o concentration expends the unit-cell volume. Adapted from [9].

4.3 Control of ferromagnetic coercive field

To investigate the V_O effect on ferromagnetic properties in SRO, we measured temperature-dependent longitudinal resistivity and magnetization for both STO(100 mTorr)/SRO and STO(5 mTorr)/SRO (**Fig. 4-4**). They show paramagnetic-ferromagnetic transitions at T_C~150 K.

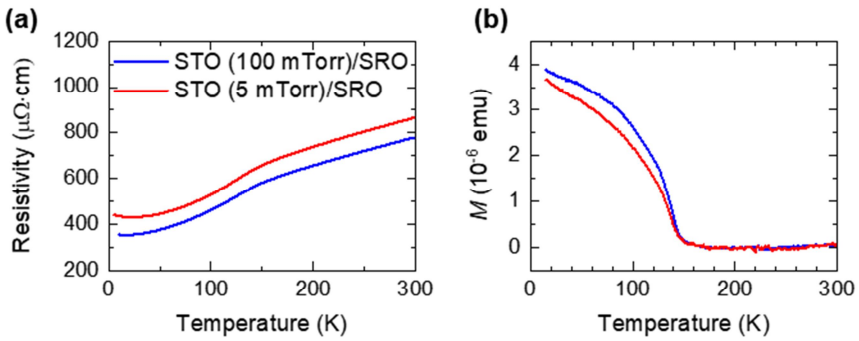

Fig. 4-4. Transport and magnetization measurement of STO/SRO thin films. **a** Temperature-dependent longitudinal transport (ρ_{xx}-T) measurement of STO(100 mTorr)/SRO and STO(5 mTorr)/SRO. **b** Temperature-dependent magnetization (M-T) measurement of STO(100 mTorr)/SRO and STO(5 mTorr)/SRO. The Curie temperature (T_C) of the ferromagnetic transition is indicated by the kinks in ρ_{xx}-T and M-T. T_C of both films is about 150 K. Adapted from [9].

To closely look at magnetic switching behavior, we measured the anomalous Hall effect (AHE). Due to time-reversal symmetry breaking of ferromagnetism, AHE can give magnetic hysteresis. Then, Hall resistivity (ρ_{xy}) of ferromagnetic SRO can be described by $\rho_{xy} = \rho_{OHE} + \rho_{AHE}$, where ρ_{OHE} and ρ_{AHE} are the ordinary and anomalous Hall resistivities[10]. For precisely determining the magnetic coercive field (H_C), we first subtracted the ρ_{OHE} component by linear fitting the ρ_{xy}-H curves at the $\mu_0 H > 4$ T, and then normalized the ρ_{AHE}-H curve using the saturated ρ_{AHE} value at 5 T.

Fig. 4-5 shows that continuous control of magnetic coercive field (H_C) in the SRO layer was possible depending on amount of V_O. The amount of V_O was controlled with various t_{STO} and $P(O_2)_{STO}$. The H_C of the STO(5 mTorr)/SRO samples increases with thicker t_{STO} or smaller $P(O_2)_{STO}$ at 5 K. The H_C of the STO/SRO sample (t_{STO} = 10 u.c., $P(O_2)_{STO}$ = 5 mTorr) is enlarged by 200%. Such a significant enhancement in H_C has rarely been achieved in SRO systems or other ferromagnetic oxides. It indicates that control of V_O is effective ways to tune H_C.

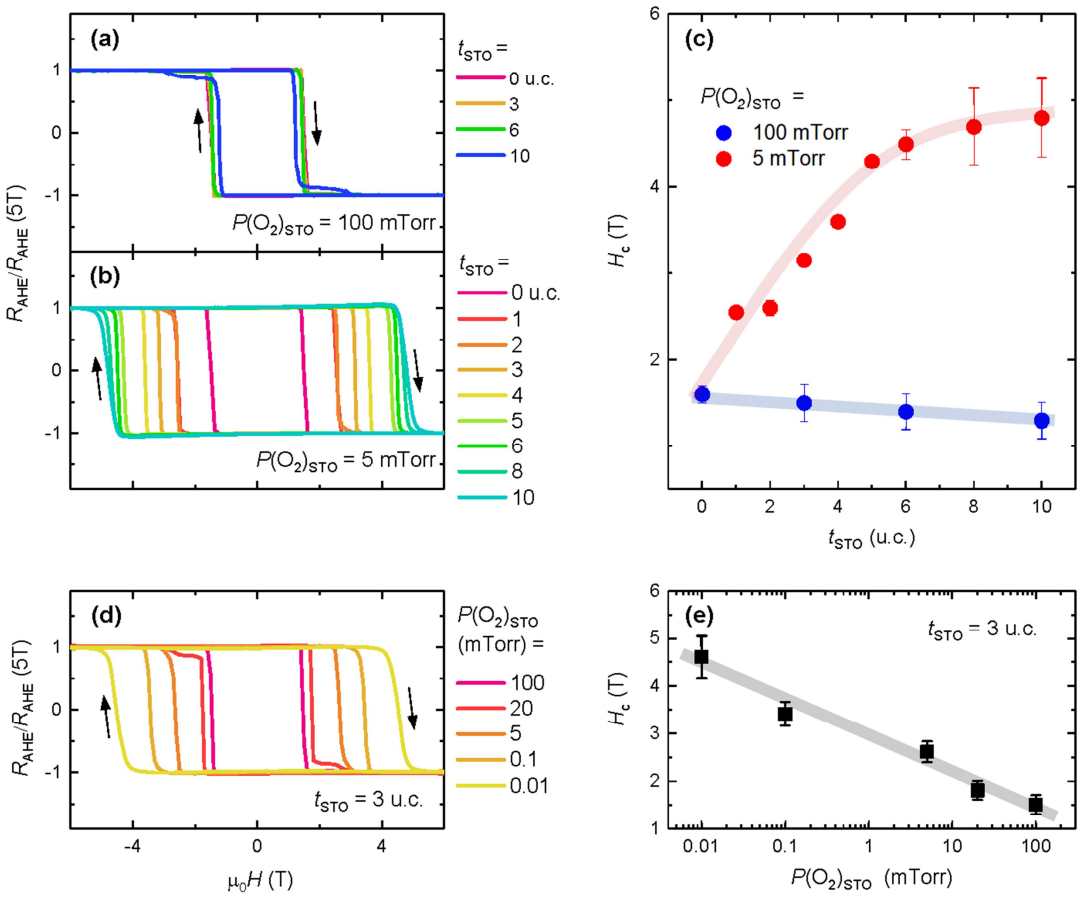

Fig. 4-5. The variation of the coercive field (H_C) with thickness of capping STO (t_{STO}) and $P(O_2)_{STO}$. **a** Normalized H-dependent anomalous Hall resistivity (ρ_{AHE}-H) measured at 5 K in STO(100 mTorr)/SRO for different t_{STO}. There is little change of H_C with t_{STO}. **b** Normalized ρ_{AHE}-H measured at 5 K in STO(5 mTorr)/SRO for different t_{STO}. Contrary to (**a**), there is a large increase of H_C as t_{STO} increases. c) t_{STO} dependent H_C of STO/SRO

with $P(O_2)_{STO}$ = 100 mTorr (solid blue circles) and $P(O_2)_{STO}$ = 5 mTorr (solid red circles). H_C decreases slightly as t_{STO} increases for $P(O_2)_{STO}$ = 100 mTorr, whereas H_C grad ually increases from 1.6 to 4.8 T and then saturates for $P(O_2)_{STO}$ = 5 mTorr. **d** Normalized ρ_{AHE}-H measured at 5 K in STO (t_{STO}=3 u.c.)/SRO with different $P(O_2)_{STO}$. H_C greatly increases for decreasing $P(O_2)_{STO}$. **e** $P(O_2)_{STO}$ dependent H_C of SRO. H_C varies significantly by changing $P(O_2)_{STO}$. Adapted from [9].

To understand the origin of H_C enhancement, we investigated direction and magnitude of MA for the films by using field-angle dependent experiments[11,12]. **Fig. 4-6** shows results of field-angle dependent ρ_{xy}. External magnetic field (H) rotates in the (100) plane for both in the clockwise and anticlockwise directions. The angle of H is denoted as θ. The center position of hysteresis, which is due to magnetic switching, is located at 90° or 270°. This indicates that easy axis of our SRO films is out-of-plane. In other words, the SRO films have perpendicular MA (PMA).

To further analyze PMA of the samples, we took the first order derivative of ρ_{xy}-θ results. Then we extracted two parameters: $\Delta\theta_{flip}$ and ρ_{slope}. We defined $\Delta\theta_{flip}$ as the difference in θ values where the magnetic switching occurs. The ρ_{slope} is defined as the maximum value of $d\rho_{xy}/d\theta$. Both parameters are sensitive to the relative strength of MA. In the case for large PMA materials, the magnetization will always prefer to align with the out-of-plane axis. Then magnetic switching occurs when the out-of-plane component of H ($H\cos\theta$) reverses, giving a sharp switching. It will give large hysteresis with large $\Delta\theta_{flip}$ and ρ_{slope}. With small PMA, however, the direction of magnetization tends to follow that of H. This continuous reorientation of magnetization will give smaller $\Delta\theta_{flip}$ and $\rho_{slope.}$

V_O concentration in ultrathin SRO films changed magnitude of PMA. For the SRO sample with little V_O concentration (STO(100 mTorr)/SRO), both $\Delta\theta_{flip}$ and ρ_{slope} become suppressed as H increases. It indicates at higher H, the continuous reorientation of magnetization happens. On the other hand, with large amount of V_O in SRO (for the STO(5 mTorr)/SRO sample), the $\Delta\theta_{flip}$, and the ρ_{slope} varies slower and remains unchanged as H increases. This result suggests a sharp magnetic switching until large $H \sim$

14 T.

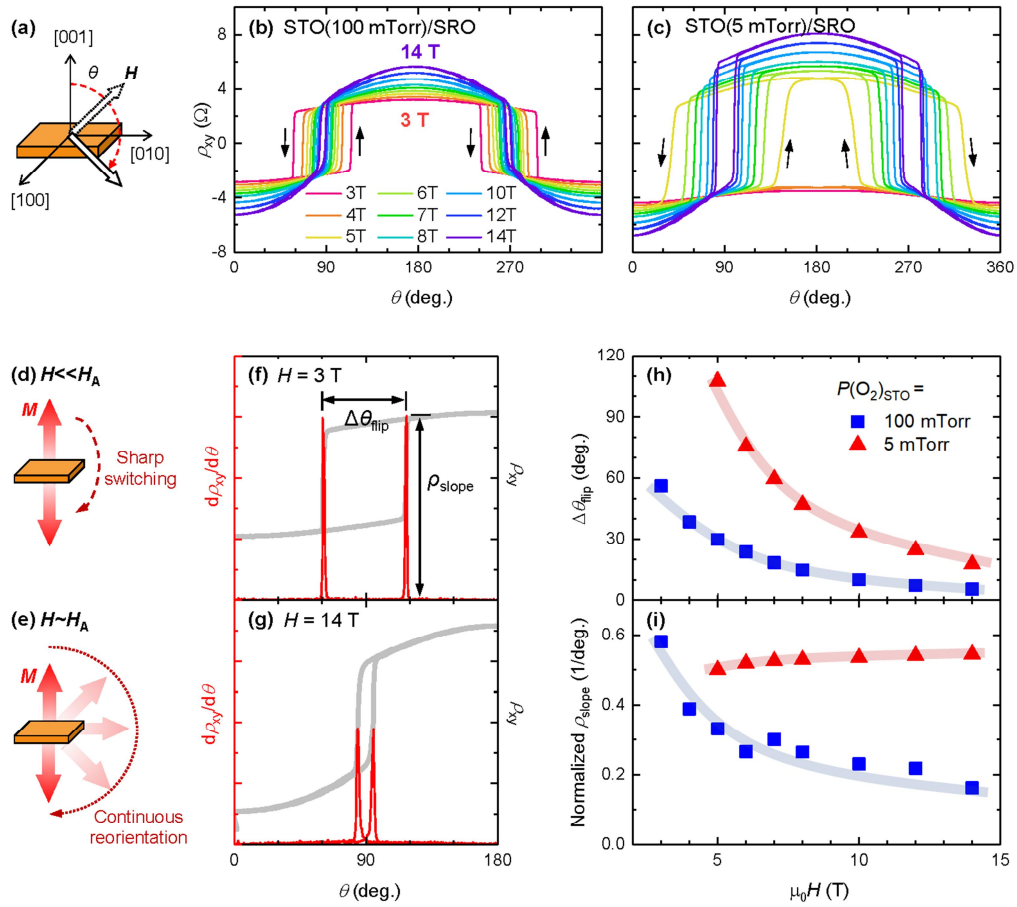

Fig. 4-6. Measurement of magnetic anisotropy by field-angle dependent Hall effect. **a** Experimental geometry of field-angle dependent Hall resistivity (ρ_{xy}). The angle between the external field (H) and [001] axis is denoted as θ. **b, c** The field angle dependent Hall resistivity (θ-ρ_{xy}) of (**b**) STO(100 mTorr)/SRO and (**c**) STO(5 mTorr)/SRO(5 u.c.) at 5 K. A constant H rotates both clockwise and anticlockwise. **d, e** Schematic magnetization configurations of SRO when (**d**) H is much smaller than the anisotropy field (H_A) and (**e**)

H is comparable to H_A. When $H<<H_A$, the magnetization aligns with the film normal, showing a large hysteresis area with sharp magnetic switching. By contrast, when H is comparable to H_A, the spin will continuously reorient along the H direction, showing a smaller hysteresis area and smooth magnetic switching. **f, g** $d\rho_{xy}/d\theta$ - θ curves when (**f**) $H<<H_A$ [H = 3T for STO(100 mTorr)/SRO] and (**g**) $H\sim H_A$ [H =14T for STO(100 mTorr)/SRO]. $\Delta\theta_{flipping}$ is the difference in θ where magnetic switching occurs. ρ_{slope} is the peak value of $d\rho_{xy}/d\theta$. **h** H dependent $\Delta\theta_{flipping}$ of both samples. **i** Normalized H dependent ρ_{slope} for both films. The larger values of both $\Delta\theta_{flipping}$ and ρ_{slope} for STO(5 mTorr)/SRO at high H indicate that H_A of STO(5 mTorr)/SRO is larger than that of STO(100 mTorr)/SRO. Adapted from [9].

There can be two collaborative mechanisms for explaining for the enhancement of PMA. First, the high-density V_O can expand the out-of-plane lattice of SRO. Such structural distortion can enhance the magnetocrystalline anisotropy, thus leading to larger PMA[13–15]. Second, the point defects may act as pinning sites and change the domain wall propagation speed. Accordingly, the stronger defect pinning of domain walls in the oxygen-deficient STO/SRO film will enlarge H_C.

4.4 Conclusion

We suggested an effective method for V_O migration in STO/SRO heterostructures and controlled their PMA. During PLD of STO capping layer, kinetic energy of adatoms which arrive on the surface of the underneath SRO can be controlled by growth pressure. We could control amount of V_O which migrates from STO capping layer to the SRO layer. Our method realized a wide range modulation of PMA.

We believe controlling V_O in ultrathin TMOs holds great potential for investigating both fundamental physics and device applications. Our method can induce inversion-symmetry breaking, giving large difference of *c/a* ratio (~ 3 %) depending on the atomic rows. In addition, considering the wide usage of itinerant ferromagnetic SRO, control of PMA will facilitate all-oxides-based spintronic devices.

References

1. Wang, Z. *et al.* Tailoring the nature and strength of electron-phonon interactions in the SrTiO3 (001) 2D electron liquid. *Nat. Mater.* **15**, 835–839 (2016).

2. Meevasana, W. *et al.* Creation and control of a two-dimensional electron liquid at the bare SrTiO3 surface. *Nat. Mater.* **10**, 114–118 (2011).

3. Waser, R. & Aono, M. Nanoionics-based resistive switching memories. *Nat. Mater.* **6**, 833–839 (2007).

4. Lee, J. S., Lee, S. & Noh, T. W. Resistive switching phenomena: A review of statistical physics approaches. *Appl. Phys. Rev.* **2**, (2015).

5. Li, D. *et al.* Superconductivity in an infinite-layer nickelate. *Nature* **572**, 624–627 (2019).

6. Koster, G. *et al.* Structure, physical properties, and applications of SrRuO3 thin films. *Rev. Mod. Phys.* **84**, 253–298 (2012).

7. Lee, H. N., Christen, H. M., Chisholm, M. F., Rouleau, C. M. & Lowndes, D. H. Thermal stability of epitaxial SrRuO3 films as a function of oxygen pressure. *Appl. Phys. Lett.* **84**, 4107–4109 (2004).

8. Jeon, S. H., Park, B. H., Lee, J., Lee, B. & Han, S. First-principles modeling of resistance switching in perovskite oxide material. *Appl. Phys. Lett.* **89**, 042904

(2006).

9. Ko, E. K. *et al.* Oxygen Vacancy Engineering for Highly Tunable Ferromagnetic Properties: A Case of SrRuO3 Ultrathin Film with a SrTiO3 Capping Layer. *Adv. Funct. Mater.* **30**, 2001486 (2020).

10. Nagaosa, N., Sinova, J., Onoda, S., MacDonald, A. H. & Ong, N. P. Anomalous Hall effect. *Rev. Mod. Phys.* **82**, 1539–1592 (2010).

11. Kan, D. *et al.* Tuning magnetic anisotropy by interfacially engineering the oxygen coordination environment in a transition metal oxide. *Nat. Mater.* **15**, 432–437 (2016).

12. Kan, D., Aso, R., Kurata, H. & Shimakawa, Y. Thickness-dependent structure-property relationships in strained (110) SrRuO3 Thin Films. *Adv. Funct. Mater.* **23**, 1129–1136 (2013).

13. Gan, Q., Rao, R. A., Eom, C. B., Garrett, J. L. & Lee, M. Direct measurement of strain effects on magnetic and electrical properties of epitaxial SrRuO3 thin films. *Appl. Phys. Lett.* **72**, 978–980 (1998).

14. Wang, X. W. *et al.* Magnetic anisotropy and transport properties of 70 nm SrRuO3 films grown on different substrates. *J. Appl. Phys.* **109**, 07D707 (2011).

15. Harano, T. *et al.* Role of doped Ru in coercivity-enhanced La0.6Sr 0.4MnO3 thin

film studied by x-ray magnetic circular dichroism. *Appl. Phys. Lett.* **102**, 222404 (2013).

Chapter 5

Hetero-interfacial control for two-channel anomalous Hall effect

With broken time-reversal symmetry, the Berry curvature becomes non-zero, inducing anomalous Hall conductivity. As an itinerant ferromagnet, $SrRuO_3$ can be a good system for studying the relation between anomalous Hall effect (AHE) and electronic structures. Due to the complex band structures of SRO, Berry curvatures can be significantly changed by very subtle modulations of the system. Here, we provide the relation between magnetic domains and multiple-channel AHE. By utilizing hetero-interfacial engineering, we induce two different magnetic phases in SRO films.

5.1 Introduction

5.1.1 Berry curvatures and anomalous Hall effect in $SrRuO_3$

In band structure of solids, Berry phase can be non-zero with broken time-inversion symmetry or broken spatial-inversion symmetry. Such Berry phase in momentum space can have anomalous velocity, which is perpendicular to the external electric field, inducing the anomalous Hall effect (AHE). In a ferromagnet (broken time-reversal symmetry) $SrRuO_3$ (SRO), Berry curvature is non-zero and the nodal structures due to spin-orbital coupling can enhance Berry curvature[1]. Recently, it has been shown that such nodal structures can be protected even in quasi-two-dimensional SRO system[2].

SRO is good system for studying relation between AHE and electronic structures. Depending on subtle changes of degrees of freedom such as lattice, spin, or orbital, the magnitude or sign of AHE can be significantly modulated. For example, the magnitude of magnetization has been known to be related to sign of AHE[1]. The magnetic skyrmions, swirling ferromagnetic textures in real-space, can also contribute to Hall effect, leaving 'hump anomaly' in AHE[3,4]. On the other hand, motivated by the 'hump anomaly' in AHE, multiple-channel AHE interpretation have been investigated[9]. Many studies on AHE in ultrathin SRO films have been investigated with the thickness[5,6], strain[7], and structure[8] dependency.

5.2 Two different magnetic phases and two-channel anomalous Hall effect

In this study, we systematically control the two different magnetic phases in SRO ultrathin films. We grow several SRO films under identical conditions using pulsed laser deposition (PLD). We then deposit $LaAlO_3$ (LAO) layers under different oxygen pressures for manipulation of the deposition kinetics. Even when the growth conditions and thicknesses of the SRO layers were the same, simple variation of the LAO growth pressure triggers significant magnetic properties and the AHE signals. By investigating the composition of different magnetic phases with the AHE results, we find that the 'hump' signal could be explained by the two-channel AHEs.

We measure the magnetotransport and magnetic properties for LAO/SRO heterostructures (**Fig. 5-1**). For bare SRO film, there is negative sign of AHE without hump anomaly. In the magnetization-temperature (*M-T*) curves, there is one Curie temperature (T_C) near 120 K, suggesting that there is single magnetic phase. Interestingly, the AHEs and magnetic properties of LAO/SRO films are affected by the oxygen pressure during the growth of the top LAO insulating layer [$P(O_2)_{LAO}$]. When the $P(O_2)_{LAO}$ is decreased, the sign of AHE signal flips from negative to positive and a small hump anomaly arises during sign change. The *M-T* curves exhibit two T_C around ~120 and ~90 K, suggesting the two different magnetic phases. When $P(O_2)_{LAO}$ becomes lower, the regions with the ~120 K magnetic vanish and those with the lower T_C become dominant.

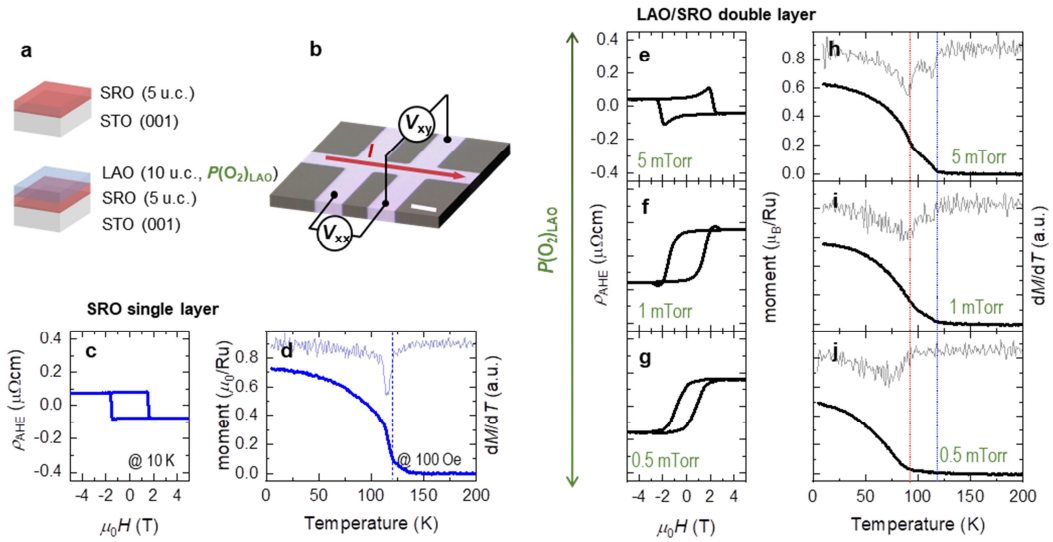

Fig. 5-1. Field-dependent anomalous Hall resistivity (ρ_{AHE}-H) curves and temperature-dependent magnetization (M-T) curves of $SrRuO_3$ (SRO) and $LaAlO_3$ (LAO)-capped SRO films. **a** 5 u.c.-SRO films and with and without the capping layers. **b** Optical microscopic image of 50×50 ic^2 Hall bar. The scale bar indicates 50 μm. **c** ρ_{AHE}-H curves of 5 u.c.-SRO films without capping layers measured at 10 K. All linear terms from the ordinary Hall effect have been subtracted. **d** M-T curves of 5 u.c.-SRO films without capping layers. The black solid lines are the experimental data and the grey solid lines are the first derivative curves. **e-g** ρ_{AHE}-H curves of LAO-capped SRO films. The growth conditions and thicknesses of the SRO layers were fixed while the oxygen pressure during LAO layer growth [$P(O_2)_{LAO}$] was varied from 5 to 0.5 mTorr. **h-j** M-T curves of LAO-capped SRO films. The blue (red) dotted lines were derived at Curie temperatures (T_C) of ~120 K (~90 K). Adapted from [10].

To confirm two different regions, we perform scanning transmission electron microscopy (STEM) in annular bright-field (ABF) mode. **Fig. 5-2** shows STEM-ABF images of LAO/SRO films grown with $P(O_2)_{LAO}$ = 5 and 0.5 mTorr, respectively. For the $P(O_2)_{LAO}$ = 5 mTorr film, the STEM-ABF image is uniform with well-defined atomic peaks. However, the $P(O_2)_{LAO}$ = 0.5 mTorr film exhibits nonuniform contrast, suggesting nanoscale inhomogeneities. When LAO is deposited at higher oxygen pressure, the SRO layer is relatively uniform in structure, with little deformation. On the other hand, when LAO is deposited at lower pressure, the SRO atomic peaks have irregular patterns (marked by the red-dashed circle). We can conclude that the SRO layer is deformed when the LAO capping layer are grown at lower oxygen pressure.

We next perform depth-profile measurements using time-of-flight secondary ion mass spectrometry (TOF-SIMS). The LAO/SRO samples are etched with Cs (from the top) during cation mass analysis. We obtain stoichiometric depth profiles, and compare the TOF-SIMS data of LAO-capped SRO samples created at $P(O_2)_{LAO}$ values of 5 and 0.5 mTorr. During the initial sputtering time (0~250 s), signals from the LAO capping layer only are observed. The TOF spectra of La differ by 15.0%; those of Al do not exhibit any difference. After sputtering for 250 s, atoms of the SRO layer begin to contribute to the TOF spectra. Compared to the LAO layer, the stoichiometric modification is much more severe in the SRO layer. The difference is 9.3% for the Sr spectra and 31.5% for the Ru spectra, indicating many Ru deficiencies in the SRO film when a low $P(O_2)_{LAO}$ is used.

Note that Ru deficiencies in SRO degrade itinerant ferromagnetism, causing AHE sign reversal. We found that Ru deficiencies introduced during LAO layer formation caused nanoscale structural deformations of the SRO layer, decreased T_C, and rendered ρ_{AHE} positive. Such stoichiometric changes and structural deformations explain the coexistence of SRO nano-regions with different magnetic properties.

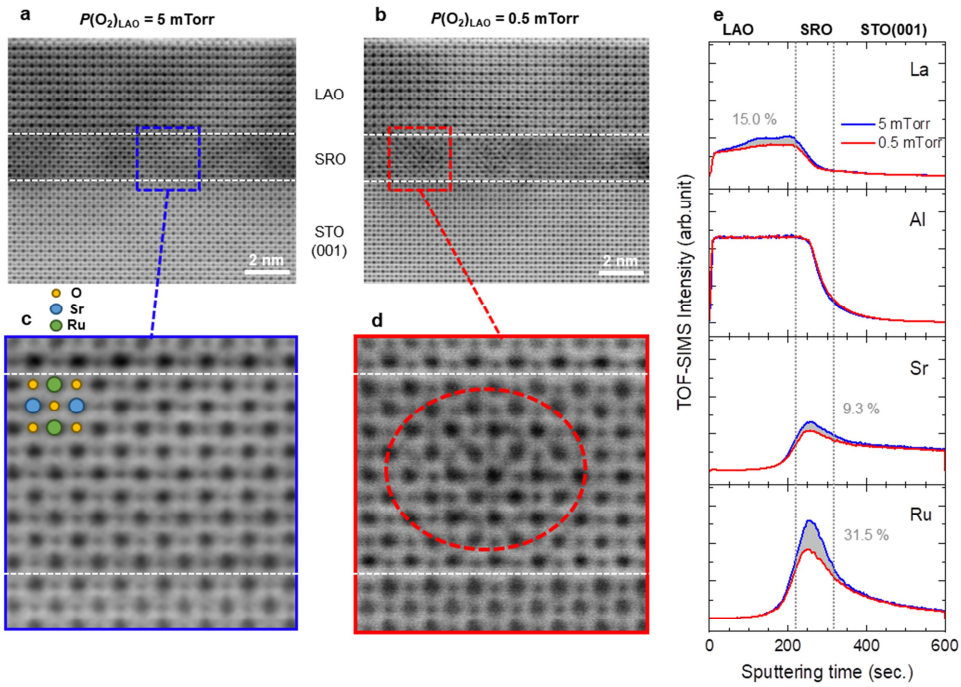

Fig. 5-2. Scanning transmission electron microscopy (STEM) images, obtained in annular bright-field (ABF) mode, of LAO-capped SRO films, and their time-of-flight secondary ion mass spectra (TOF-SIMS). **a, b** STEM images of LAO-capped SRO when $P(O_2)_{LAO}$ = 5 mTorr (**a**) and 0.5 mTorr (**b**). **c** Enlarged image of the blue dashed square in (**a**). **d** Enlarged images of the red dashed square in (**b**). The atomic positions of cations and oxygens are well-defined in the $P(O_2)_{LAO}$ = 5 mTorr sample, but not in the $P(O_2)_{LAO}$ = 0.5 mTorr sample. The elongation and uncertainty of positioning is highlighted in red dashes. **e** Depth profile of the TOF-SIMS. The blue solid line is that from the $P(O_2)_{LAO}$ = 5 mTorr sample and the red solid line indicates the $P(O_2)_{LAO}$ = 0.5 mTorr sample. The grey areas indicate differences between the samples. The grey digits indicate the

proportions of grey areas, as revealed by the integrated TOF spectra from the 5-mTorr sample. Ru deficiency is mainly observed in the SRO layer. Adapted from [10].

We found that the *M-T* curves of all of the LAO/SRO films could be explained using a simple two-component model. The *M-T* curves of LAO/SRO films grown with $P(O_2)_{LAO}$ = 50 and 0.5 mTorr exhibited simple monotonical decreases of *M* with *T*, and apparent T_C values around 120 and 90 K respectively (**Fig. 5-3**). For convenience, we term these the 120 and 90 K phases. If the fitting is done under the assumption that all films are composed of these two phases, we can explain the *M-T* curves of all LAO/SRO films (. The red and blue lines indicate the contributions from the 90 and 120 K phases respectively. The green lines show the sums of these two contributions, and agree well with the experimental data. The proportion of the 90 K phase (i.e., the Ru-deficient phase) increases as $P(O_2)_{LAO}$ decreases.

The simple two-component model well explains the ρ_{AHE}-*H* curves of all LAO/SRO films. If only the 120 K phase (90 K phase) exists, the AHE has a negative (positive) sign without any hump signal. However, when the two phases co-exist, the AHE hump structure appears, indicating two-channel AHE. To analyze the proportions of the two phases, we fitted ρ_{AHE}-*H* curves by combining the ρ_{AHE} curves with opposite AHE signs. The red and blue lines indicate the contributions of the 90 K and 120 K phases to ρ_{AHE}, respectively. The green lines show the sum of these two phases, in good agreement with the experiments. The little variation in the magnetic coercive field might originate from nano-scale defects. We plotted the proportions of the 90 K phase yielded by the ρ_{AHE} analysis (black line); these were quite consistent with those derived via *M-T* analysis (the orange line). This emphasizes that it is possible to tune the magnetic and magnetotransport properties of SRO layers via *in situ* deposition of an LAO capping layer.

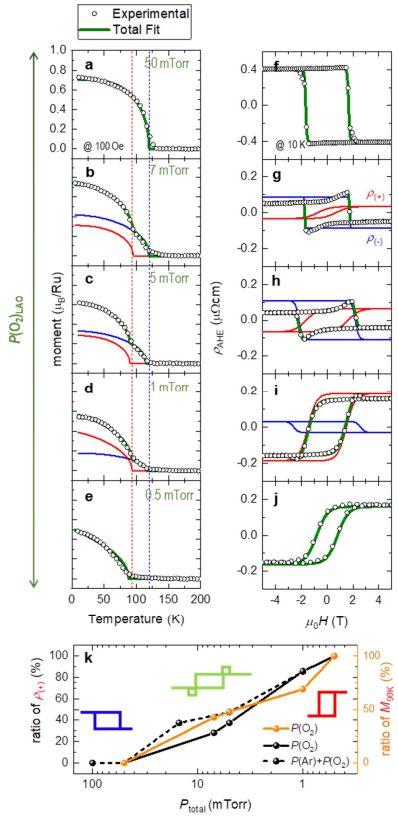

Fig. 5-3. Fitted *M*-*T* curves and ρ_{AHE}-*H* values of LAO-capped SRO samples, and the ratios of the 90 K phase. **a–e** Fitted *M*-*T* curves of LAO-capped SRO samples with $P(O_2)_{LAO}$ values of 50 (**a**), 7 (**b**), 5 (**c**), 1 (**d**), and 0.5 mTorr (**e**). The red and blue curves are fitting curves at T_C values of 90 and 120 K, respectively. Black open circles are experimental results and the green lines are the summations of the fitting curves. **f–j** The fitted ρ_{AHE}-*H* curves of LAO-capped SRO samples when the LAO layer growth pressures were 50 (**f**), 7 (**g**), 5 (**h**), 1 (**i**), and 0.5 mTorr (**j**). The red and blue curves are negative ($\rho_{(-)}$)

and positive ($\rho_{(+)}$) fitting curves. **k** The total pressure during capping layer growth (P_{total}) affects the 90 K phase ratios extracted from the fittings. The black circles are the ratios extracted from ρ_{AHE}-H curves and the orange circles are the ratios extracted from M-T curves. The solid lines are the results obtained when the LAO capping layers were grown under only oxygen pressure. The dashed line indicates the ratios of samples for which the LAO capping layers were grown in a mixture of argon and oxygen. As the $P(O_2)_{LAO}$ decreases, the 90 K phase ratio increases. Adapted from [10].

5.3 Magnetic inhomogeneity induced during heterostructure engineering

Now, we focus on the highly kinetic nature of PLD to understand the effect of the capping layer. During PLD, an incoming pulsed laser beam ablates the target and creates a plasma plume via laser-material interaction[11–13]. The plume contains highly energetic species that will be transferred to the heated substrate. Since the plume kinetics of PLD is mainly governed by the growth pressure, its effect on the film heterostructure would be systematically tunable (**Fig. 5-4**). At high pressure, plume species experience many collisions and thus exhibit low kinetic energies. These species barely damage an already deposited film. On the other hand, at low pressure, plume species collide less, thus maintaining high velocities. Plume species bombard the already deposited film, creating serious modifications. In our LAO/SRO double-layer films, a lower $P(O_2)_{LAO}$ creates Ru-deficient regions in the SRO layer, inducing an inhomogeneous (mixed) state. If the induced inhomogeneous phase has a positive AHE and a T_C around 90 K, the experimental magnetic properties can be easily explained. The positive AHE in the inhomogeneous phase gives two-channel AHEs in SRO films, thus explaining the AHE humps.

To verify our kinetics-based explanation, we performed additional control experiments using an Ar/O_2 gas mixture. With $P(O_2)_{LAO}$ fixed at 0.5 mTorr, we added Ar to increase the total pressure P_{Total} inside the chamber. We varied P_{Total} from 0.5 to 15.0 mTorr when

growing LAO (10u.c.)/SRO (5-u.c.) double-layer films. Using the two-component model described above, we fitted the ρ_{AHE}-H curves with the negative (blue) and positive (red) components. As P_{Total} decreases, the negative component decreases, and the positive component increases. The results of the control experiment are also plotted according to P_{Total}. The data are in reasonable agreement with those of the $P(O_2)_{LAO}$ control experiments, indicating that it is possible to tune the magnetotransport properties of $SrRuO_3$ ultrathin films by controlling the PLD kinetics.

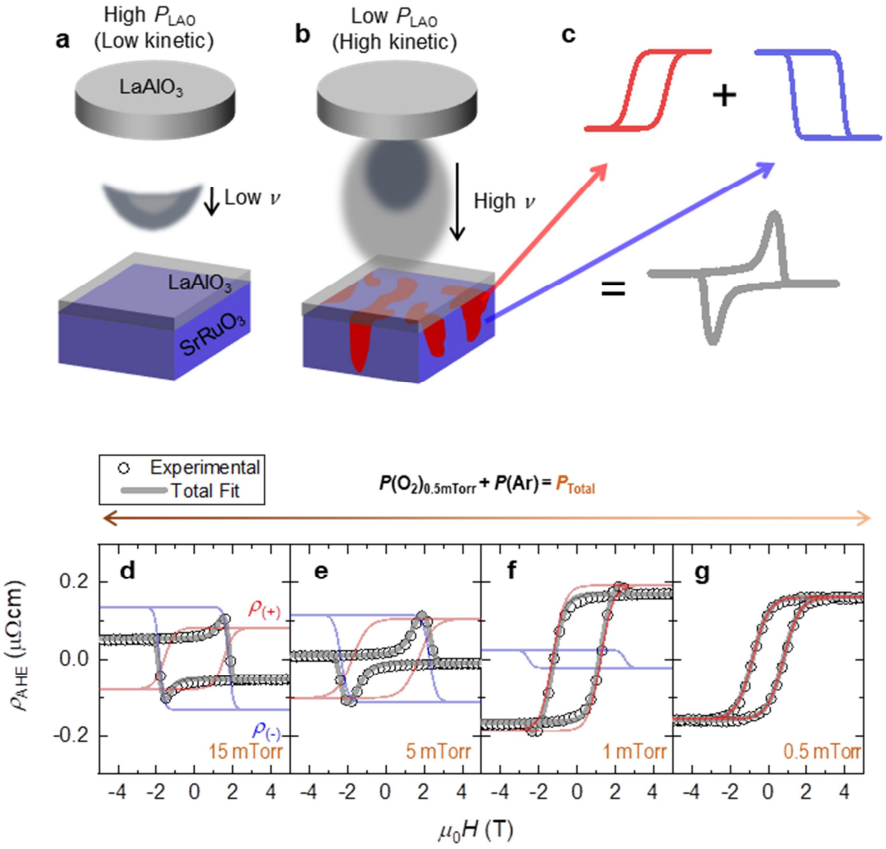

Fig. 5-4. Schematics of PLD kinetics according to the background pressure, and a

control experiment with total pressure variation during growth of the LAO capping layer. **a** At high pressure, the kinetic energy of the evaporated plume is suppressed. **b** At low pressure, the high kinetic energy of the evaporated plume induces SRO film inhomogeneities. The red regions in the SRO layer re inhomogeneous phases caused by the high kinetic energy of the adatoms. **c** The red regions in the SRO film exhibit positive AHEs, as shown by the hump signals in the ρ_{AHE}-H curve. **d–g** ρ_{AHE}-H curves derived by varying P_{Total} from 15 to 0.5 mTorr. The O_2 partial pressure is fixed at 0.5 mTorr; only the Ar partial pressure is varied. The black open circles are the experimental curves and the red and blue curves the $\rho_{(-)}$- and $\rho_{(+)}$-fitting curves. The gray lines are the summations of the fitting curves. As P_{Total} decreases, $\rho_{(+)}$ increases. Adapted from [10].

The *M-T* curves of the P_{Total} control experiments are similar to those of the $P(O_2)_{LAO}$ control experiments (**Fig. 5-5**) in terms of pressure dependence. When an AHE hump is observed, the *M-T* curves indicate the coexistence of the so-called 90 and 120 K phases. Therefore, our work suggests that bombardment by highly kinetic species in the plume explains the Ru deficiencies in the SRO layer developing during LAO deposition.

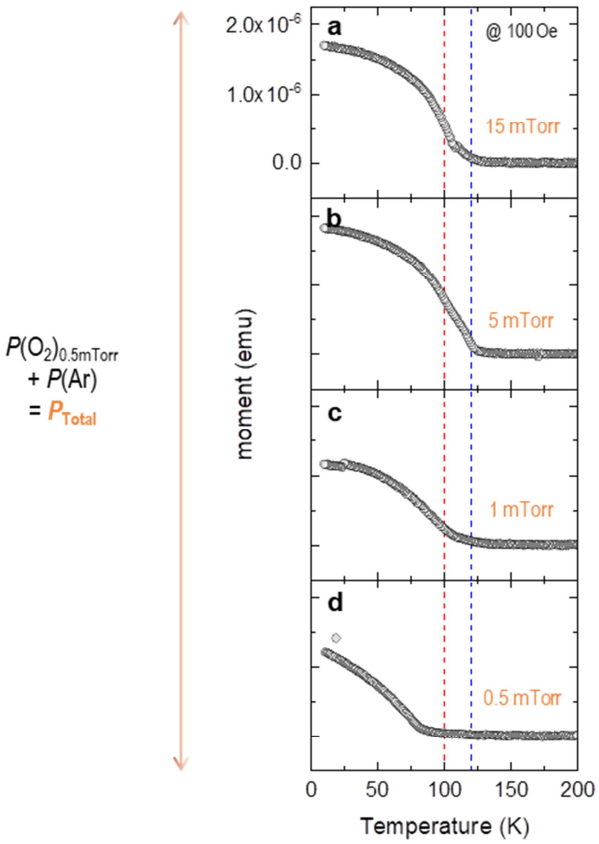

Fig. 5-5. Temperature dependence of magnetization (*M-T*) of a control experiment with

total pressure (P_{total}) variation during the growth of the LAO capping layer. P_{Total} is varied from 15 mTorr to 0.5 mTorr. The O_2 partial pressure is fixed as 0.5mTorr, while Ar partial pressure is only varied. Adapted from [10].

5.4 Conclusion

We systematically investigated changes in the magnetic and two-channel AHEs of LAO/SRO double-layer films by utilizing the high-kinetic nature of PLD. The growth pressure of the LAO capping layer is a crucial parameter for tuning the amount of different magnetic domains. When the pressure is low, high-kinetic species transported during LAO deposition can modify the SRO layer. Our STEM and TOF-SIMS studies revealed inhomogeneous, nanoscale SRO regions of structural deformation and Ru-deficiency, which can change the magnetic properties. The coexistence of inhomogeneous regions yields two-channel AHE signals, i.e., the hump anomalies.

Our work emphasizes the importance of in-depth exploration of high-kinetic PLD when creating oxide heterostructures. These exhibit intriguing physical properties, including multiple layers and superlattices. The highly kinetic bombardment generates nanoscale structural and compositional deformations, which significantly affect the macroscopic properties. Careful control of the kinetics allows for simple and effective tuning of the various properties of PLD-grown oxide heterostructures.

References

1. Fang, Z. *et al.* The anomalous Hall effect and magnetic monopoles in momentum space. *Science (80-.).* **302**, 92–95 (2003).

2. Sohn, B. *et al.* Sign-tunable anomalous Hall effect induced by two-dimensional symmetry-protected nodal structures in ferromagnetic perovskite thin films. *Nat. Mater.* **20**, 1643–1649 (2021).

3. Matsuno, J. *et al.* Interface-driven topological Hall effect in SrRuO3-SrIrO3 bilayer. *Sci. Adv.* **2**, e1600304 (2016).

4. Wang, L. *et al.* Ferroelectrically tunable magnetic skyrmions in ultrathin oxide heterostructures. *Nat. Mater.* **17**, 1087–1094 (2018).

5. Wang, L. *et al.* Controllable Thickness Inhomogeneity and Berry Curvature Engineering of Anomalous Hall Effect in SrRuO3 Ultrathin Films. *Nano Lett.* **20**, 2468–2477 (2020).

6. Kimbell, G. *et al.* Two-channel anomalous Hall effect in SrRuO3. *Phys. Rev. Mater.* **4**, 054414 (2020).

7. Tian, D. *et al.* Manipulating Berry curvature of SrRuO3 thin films via epitaxial strain. *Proc. Natl. Acad. Sci. U. S. A.* **118**, 1–7 (2021).

8. Miao, L. *et al.* Strain relaxation induced transverse resistivity anomalies in

SrRuO3 thin films. *Phys. Rev. B* **102**, 064406 (2020).

9. Kimbell, G., Kim, C., Wu, W., Cuoco, M. & Robinson, J. W. A. Challenges in identifying chiral spin textures via the topological Hall effect. *Commun. Mater.* **3**, (2022).

10. Ko, E. K. *et al.* Tunable Two-Channel Magnetotransport in SrRuO3 Ultrathin Films Achieved by Controlling the Kinetics of Heterostructure Deposition. *Adv. Electron. Mater.* **8**, 1–8 (2022).

11. Eason, R. *Pulsed Laser Deposition of Thin Films*. (Wiley-Interscience, 2006).

12. Leboeuf, J. N. *et al.* Modeling of plume dynamics in laser ablation processes for thin film deposition of materials. *Phys. Plasmas* **3**, 2203 (1996).

13. Lafane, S. *et al.* Correlation of plume dynamics and oxygen pressure with VO2 stoichiometry during pulsed laser deposition. *Appl. Phys. A Mater. Sci. Process.* **112**, 159 (2013).

Chapter 6

Summary and Outlook

In this chapter, we summarize the research results in this thesis, providing outlook for further studies related to this works. The main goal for this thesis is to study hetero-interfacial effect on $SrRuO_3$ (SRO) ultrathin film. For this purpose, we use utilize strain engineering on SRO monolayer by using different substrates. We also utilize capping layer effect on ultrathin SRO films.

In **chapter 3**, we demonstrated the strain engineering on SRO monolayer with symmetry-preserving method. The original triple degenerate t_{2g} orbitals lifted due to the tetragonal crystal field splitting. This resulted in a Mott transition, which occurred with concurrent opening of a band insulating and a Mott gap. We showed orbital differentiation via using angle-resolved photoemission spectroscopy (ARPES). Our results suggested that strain engineering in two-dimensional systems can be an effective method for investigating multi-orbital physics.

In **chapter 4**, we showed the phases, which were difficult to make, could be stabilized via hetero-interfacial engineering. The realization of the phase of SRO with oxygen vacancy (V_O) has been hampered by volatility of Ru. By depositing oxygen-deficient $SrTiO_3$ (STO) on SRO, we utilized V_O migration at the STO/SRO. The high kinetic

process during PLD helped for V_O to overcome the migration barrier. The amount of V_O migration could be modulated by growth pressure during capping layer deposition. We also discussed that large amount of V_O enhanced ferromagnetic coercive field and perpendicular magnetic anisotropy in SRO ultrathin films.

In **chapter 5**, we discussed on the relation between magnetic properties and anomalous Hall effect (AHE) in ultrathin SRO films. The two different magnetic domains in SRO ultrathin films were induced and the portion was controlled by deposition of $LaAlO_3$ capping layers. Then we successfully interpreted the AHE results with two-channel AHE. This indicates the magnetic property in ultrathin SRO films is closely related to the AHE.

Throughout this thesis, we suggest hetero-interfacial engineering methods using PLD such as symmetry-preserving strain engineering, and control of kinetic process during capping layer growth. These methods can be utilized to other TMOs for investigating functional properties and electronic correlations by modulating degrees of freedom systematically.

Curriculum Vitae

Eun Kyo Ko

B. S. degree

Ewha Womens University, Seoul, Korea (2012 ~ 2017)

Double major in Physics and Chemistry

Ph. D degree

Department of Physics and Astronomy, Seoul National University (2017 ~)

Supervised by Prof. Tae Won Noh

Awards and Activities

- Best oral presentation award, Korean Physical Society Spring meeting, Korea, 2022
- Outstanding Graduate Student Award, The Korean Magnetic Society, 2022
- Brain Korea Doctoral Scholarship, 2022
- Gold award for the best oral presentation in young researcher competition,

Oxide Superspin, Kyoto, Japan, 2021

- The thesis award, National Center for Inter-University Research Facilities, Korea, 2021
- Brain Korea Doctoral Scholarship, 2020
- Best poster award, Korean Physical Society Fall meeting, Korea, 2020
- Best poster award, Dielectric Symposium Muju, Korea 2019
- Best poster award, Oxide Superspin International School Sapporo, Japan, 2018
- Best poster award, Oxide Superspin Amalfi, Italy, 2018
- Ewha-Luce international seminar (ELIS: Expanding Horizons), 2018

List of Publication

[1] Strain engineering for orbital-selective phase transition in a two-dimensional Hund's correlated system

E. K. Ko*, S. Hahn*, C. Sohn, S. Lee, B. Sohn, J. R. Kim, J. Son, Y. Kim, D. Kim, M. Kim, C. H. Kim, C. Kim, and T. W. Noh

In preparation

[2] Quantitative iDPC-STEM observations of oxygen octahedral connectivity control at perovskite oxide interfaces via epitaxial strain engineering

J. Mun*, E. K. Ko*, W. Peng, T. W. Noh, and M. Kim

In preparation

[3] Nanoscale enhancement of optical conductivity near cracks due to strain relaxation

C. J. Roh*, E. K. Ko*, Y. Chang*, S. H. Park, J. Mun, M. Kim, and T. W. Noh

In preparation

[4] Higher harmonics in planar Hall effect induced by cluster magnetic multipoles

J. Song, T. Oh, E. K. Ko, J. H. Lee, W. J. Kim, Y. Zhu, B. J. Yang, Y. Li, and T. W. Noh

Under review (Nature Communications)

[5] Kitaev quantum spin liquid in heterostructure

B. Kang, M. Park, S. Noh, D. Choe, M. Kim, M. Kong, C. Seo, E. K. Ko, G. Yi, J. Yoo, E. Moon, J. Ok, and C. Sohn

Submitted

[6] Flexo-polar phase transition in a metal

W. Peng, S. Y. Park, J. Mun, H. Ju, L. Qu, C. J. Roh, J. Kim, E. K. Ko, S. Hahn, L. Si, J. Lee, M. Kim, C. Kim, L. Wang, T. W. Noh, and D. Lee

arXiv:2203.03199

[7] Interface control of Fermi liquid, Hund's metal, and Mott insulator in atomic-scale epitaxial oxide heterostructures

J. R. Kim, B. Sohn, H. J. Lee, S. Lee, E. K. Ko, S. Hahn, S. Lee, Y. Kim, D. Kim, H. J. Kim, Y. Kim, J. Son, C. H. Ahn, R. J. Walker, A. Go, M. Kim, C. H. Kim, C. Kim, and T. W. Noh

arXiv:2203.04244

[8] An optimized scheme for detecting magneto-optic effects in ultrathin films with Sagnac interferometry

X. D. Zhu, E. K. Ko, G. Kimbell, and J. W. A. Robinson

Submitted

[9] Tunable two-channel magnetotransport in $SrRuO_3$ ultrathin films achieved by controlling the kinetics of heterostructure deposition

E. K. Ko*, H. G. Lee*, S. Lee, J. Mun, J. Kim, J. H. Lee, T. H. Kim, J.-S. Chung, M. Kim, S. H. Chang, and T. W. Noh

Advanced Electronic Materials 8, 2100804 (2022).

[10] Superconducting Sr_2RuO_4 thin films without out-of-phase boundaries by higher-order Ruddlesden-Popper intergrowth

J. Kim, J. Mun, C. M. P. Garcia, B. Kim, R. S. Perry, Y. Jo, H. Im, H. G. Lee, E. K. Ko, S. H. Chang, S. B. Chung, M. Kim, J. W. A. Robinson, S. Yonezawa, Y. Maeno, L. Wang, and T. W. Noh

Nano Letters 21, 4185 (2021).

[11] Oxygen Vacancy Engineering for Highly Tunable Ferromagnetic Properties: A Case of $SrRuO_3$ Ultrathin Film with a $SrTiO_3$ Capping Layer

E. K. Ko, J. Mun, H. G. Lee, J. Kim, J. Song, S. H. Chang, T. H. Kim, S. B. Chung, M. Kim, L. Wang, and T. W. Noh

Advanced Functional Materials 30, 2001486 (2020).

[12] Strain-engineering of the magnetic multipole moments and anomalous Hall effect in pyrochlore iridate thin films

W. J. Kim, T. Oh, J. Song, E. K. Ko, Y. Li, J. Mun, B. Kim, J. Son, Z. Yang, Y. Kohama, M. Kim, B.-J. Yang, and T. W. Noh

Science Advances 6, eabb1539 (2020).

[13] Colossal Flexoresistance in Dielectrics

S. M. Park, B. Wang, T. Paudel, S. Y. Park, S. Das, J. R. Kim, E. K. Ko, H. G. Lee, N. Park, L. Tao, D. Suh, E. Y. Tsymbal, L.-Q. Chen, T. W. Noh, and D. Lee

Nature Communications 11, 2586 (2020).

[14] Two-channel anomalous Hall effect in $SrRuO_3$

G. Kimbell, P. Sass, B. Woltjes, E. K. Ko, T. W. Noh, W. Wu, and J. W. A. Robinson

Physical Review Materials 4, 054414 (2020).

[15] Controllable thickness inhomogeneity and Berry-curvature-engineering of anomalous Hall effect in $SrRuO_3$ ultrathin films

L. Wang, Q. Feng, H. G. Lee, E. K. Ko, Q. Lu, and T. W. Noh

Nano Letters 20, 2468 (2020).

[16] Atomic-scale Metal-Insulator Transition in $SrRuO_3$ Ultrathin Films Triggered by Surface Termination Conversion

H. G. Lee, L. Wang, L. Si, X. He, D. G. Porter, J. R. Kim, E. K. Ko, J. Kim, S. M. Park, B. Kim, A. T. S. Wee, A. Bombardi, Z. Zhong, and T. W. Noh

Advanced Materials 32, 1905815 (2020).

[17] In-operando spectroscopic ellipsometry studies of IrO_2 dynamic instabilities: Guide to in-situ growth of pyrochlore iridate thin films

W. J. Kim, E. K. Ko, S. Y. Kim, B. Kim, and T. W. Noh

Current Applied Physics 19, 400 (2019).

[18] Strong Light Confinement in Metal-Coated Si Nanopillars: Interplay of Plasmonic Effects and Geometric Resonances

S. Kim, E. Kim, Y. U. Lee, E. Ko, H.-H. Park, J. W. Wu, and D.-W. Kim

Nanoscale Research Letters 12, 151 (2017).

국문 초록 (Korean Abstract)

페로브스카이트 초박막 루테늄 산화물에서의 전자 구조에 대한 계면 제어

강상관계 물질은 비페르미 액체성, 초전도와 같은 독특한 현상을 가진다. 단일 전자 밴드 이론으로는 설명할 수 없는 이러한 현상들을 이해하기 위해 전자 간의 관계에 대해 활발하게 조사되어 왔다. 전이 금속 산화물은 강한 상관관계가 있는 시스템 중 하나이며 금속-절연체 전이, 강자성 및 초전도성과 같은 흥미로운 특성을 보인다. 이 중 $4d$ 루테늄은 전자의 상관관계를 연구하기에 적합한 시스템이다. 이 시스템에서는 쿨롱 상호작용 (U), 전자 hopping (t), 그리고 훈트 법칙 커플링 (J) 의 에너지 규모가 비슷할 수 있다. 본 학위 논문에서는 페로브스카이트 초박막 루테늄 산화물의 전자 구조를 박막의 계면 제어를 통해 조사하였다.

첫번째로, 우리는 에피택셜 응력 (epitaxial strain) 제어를 통해 $SrRuO_3$ (SRO) 하나의 층에서 훈트 법칙이 이끄는 모트 전이를 보여준다. 훈트 법칙이 이끄는 상관관계에 대한 이전의 많은 이론 연구에도 불구하고, J 값 또는 오비탈 간의 전자 분포를 실험적으로 조절하기 어려워서 실험적 확인이 거의 없었다. 여기서 우리는 J 와 결정장 (crystal field) 의 경쟁 효과를 활용하였다. 에피택셜 응력 제어는 오비탈 간의 전자 분포를 효과적으로 조절하였다. 그리고, 각도분해 광전자 분광법을 사용하여 모트 전이를 관찰하였다. 우리는 다중 오비탈 시스템에서 훈트 기반 물리를 조사하는 효과적인 방법을 제시하였다.

두번째로, 산소 결손 (oxygen vacancy) 이 있는 초박막 SRO 의 강자성 특성에 대해 논의한다. 전이 금속 산화물에서 산소 결손의 제어는 흥미로운 물리적 특성을 일으킬 수 있다. 하지만 SRO 에 산소결손을 유도하는 것은 루테늄의 높은 휘발성으로 인해 어려웠다. 여기에서 우리는 산소 결손 이동을 위해 계면 제어를 활용하였다. $SrTiO_3$ (STO) 덮음층 증착 동안 성장 압력을 변경함으로써 밑에 SRO 층에 도달하는 이온의 운동 에너지를 제어할 수 있었다. 펄스 레이저 증착 (pulsed laser deposition) 과정 중 높은 운동 에너지는 STO/SRO 계면에서 산소결손 이동 에너지 장벽을 극복할 수 있도록 도와주었다. 우리는 SRO 의 산소결손과 그에 따른 격자 변이를 관찰하였다. 그리고 초박막 SRO 의 보자력 (coercive field) 의 지속적인 제어를 산소결손 이동량을 제어하여 달성하였다. 또한 우리는 많은 양의 산소 결손이 수직 자기 이방성을 높이는 것을 확인하였다.

마지막으로, 우리는 서로 다른 자기 상 (phase) 을 유도하여 초박막 SRO 에서 다중 비정상 홀 효과를 조사하였다. $LaAlO_3$ 덮음층 성장 동안 압력을 제어하여 운동에너지를 조절하였다. 성장 압력에 따라 SRO 필름에서 두 개의 서로 다른 자기 상이 유도되었고, 이들 사이의 비율은 체계적으로 제어할 수 있었다. 우리는 비정상 홀 효과의 크기와 부호가 자기 상의 구성에 따라 변한다는 것을 발견하였다. 이 결과는 초박막 SRO 필름의 비정상 홀 효과가 자기 특성과 밀접한 관련이 있음을 나타낸다.

주요어: 전이 금속 산화물, 에피택셜 응력 제어, 계면 제어, 전자 구조, 훈트 법칙, 모트 전이, 금속-비금속 전이, 산소 결손, 강자성, 비정상 홀 효과

학번: 2017-26688